Silicon Electrolyte Interface Stabilization (SEISta)
Q1 FY19

Anthony Burrell

National Renewable Energy Laboratory
15013 Denver West Parkway
Golden, CO 80401
Phone: (303) 384-6666
E-mail: anthony.burrell@nrel.gov

Brian Cunningham, DOE-EERE-VTO Program Manager

Hybrid Electric Systems, Battery R&D
Phone: (202) 586-8055
E-mail: brian.cunningham@ee.doe.gov

Table of Contents

Project Introduction

This report documents the Silicon Electrolyte Interface Stabilization team's approach in 1) characterizing the early-stage silicon-electrolyte interphase (SEI) including progress on identifying the specific reaction pathways present in the formation of the SEI layer, and 2) establishing a procedure for measuring SEI growth rate at fixed potentials and different cycling regimes.

Silicon is a viable alternative to graphitic carbon as an electrode in lithium-ion cells and can theoretically store >3,500 mAh/g. However, lifetime problems have been observed that severely limit its use in practical systems. The major issues appear to involve the stability of the electrolyte and the uncertainty associated with the formation of a stable SEI at the electrode. Recently, calendar-life studies have indicated that the SEI may not be stable even under conditions where the cell is supposedly static. Clearly, a more foundational understanding of the nature of the silicon/electrolyte interface is required if we are to solve these complex stability issues. A new multi-lab consortium has been formed to address a critical barrier in implementing a new class of materials used in lithium-ion batteries that will allow for smaller, cheaper, and better performing batteries for electric-drive vehicles. This consortium, named the Silicon Electrolyte Interface Stabilization (SEISta) project, was formed to focus on overcoming the barrier to using such anode materials. Five national laboratories are involved: the National Renewable Energy Laboratory (NREL), Argonne National Laboratory (ANL), Lawrence Berkeley National Laboratory (LBNL), Oak Ridge National Laboratory (ORNL), and Sandia National Laboratories (SNL).

The SEISta project was specifically developed to tackle the foundational understanding of the formation and evolution of the solid-electrolyte interphase on silicon. This project will have as its primary goal an understanding of the reactivity of the silicon and lithiated silicon interface with the electrolyte in lithium-ion systems. It consists of researchers from multiple national laboratories (NREL, ANL, LBNL, ORNL, and SNL)

working toward clear unified goals. The Silicon Deep-Dive team, which focuses on the science and technology barriers in functional electrodes, is a critical partner in this work. Many of the researchers are shared between both teams, and we hold joint meetings to ensure effective communication between the teams.

The current goals of SEISta are:

Quarter 1 Milestone: Have determined if the pristine surface of the silicon influences the composition and the function of the SEI after 1, 10 and 50 cycles (XPS, SIMS, IR, and Raman, STEM, SSRM).

Quarter 2 Milestone: Have determine that the nature of the silicon surface can affect the composition, function and the thickness of the SEI.

Quarter 3 Milestone: Have determine how water concentration (as a function of water content up to 100 ppm) in the electrolyte affects SEI thickness and composition (electrochemistry, spectroscopy, impedance) of the SEI formed at 1.5, 1.0, 0.7, 0.4, 0.15 and 0.05V vs Li/Li+"

Quarter 4 Milestones: Have determine the nature of the soluble SEI components, that are formed over 10 cycles, that are soluble in the gen 2 electrolyte.

Approach

The SEISta team works to ensure that protocols for sample preparation, experimental design, and implementation as well as data reporting are consistent across the whole team. Each laboratory is working toward the same set of quarterly milestones using its own specific talents and capabilities in a concerted effort with the other team members. This joint focus results in multiple researchers interacting to produce and analyze data to ensure that individual experimental variations will not lead to erroneous results. Critical to the success of this effort is the use of standard samples that can be shared by all parties. In addition to weekly whole-team video presentations, we have held on-site face-to-face meetings each quarter for all team members and other interested parties to brainstorm and sort out issues with existing experiments and jointly develop new experimental plans.

Objectives

The critical issues that SEISta is attempting to determine are:
- What are the properties of the lithiated silicon/electrolyte interface?

- What is the silicon SEI actually made of and what reactions are contributing to it?

- How fast does the silicon SEI grow?

- Does it stop growing?

- Is it soluble?

- Can it be stabilized?

For FY19, the team continues to focus on three broad tasks:

Materials Standardization – This task is critical to the development and deployment of standardized samples and experimental procedures across the team. We will continue to provide full characterization to any new sample that is to be used for SEI studies to ensure reproducibility and full understanding of the material. This quarter's work focused on developing new oxide coatings and methods to control the thickness and density of oxide samples. In addition, work on the silicon nanoparticles has made progress with the enhancement of the

materials collection and handling system in the plasma reactor. *Although this work dominated the early part of the project and is still critical to its success, it is now only a minor part of the work and this is reflected in the relative balance of this quarterly report.*

Model Materials Development and Characterization – The nature of the electrode-electrolyte interaction in silicon electrodes is at the heart of the formation and stability of the SEI. The inherent chemical reactivity of silicon with common electrolytes has been a focus for this team and will be a primary focus moving to quarter 2. The synthesis of well-defined silicon nanoparticles and the different chemical markups of lithiated silicon surfaces is being probed by preparing model compounds and thin films that may/can exist in silicon anodes. Lithium silicides, silicates, and other inorganic material (LiF, Li_2O) are being prepared, and their reactivity with electrolytes is being determined. These materials also act as standard spectroscopy samples for the researchers who are looking at the formation of the SEI on different silicon materials.

SEI Characterization – The overall objective for SEISta is to understand the nature and evolution of the SEI on silicon anodes. The materials standardization and model compounds will enable the researchers to systematically investigate the formation of the solid-electrode interphase using a wide variety of the spectroscopy techniques—from different optical, microscopy, and electrochemistry—to determine how the SEI forms based on the nature of the silicon surface, and how it evolves over time. This section of work will continue to grow in scope as we move beyond the sample-characterization phase of the project and toward understanding the nature and evolution of the SEI. *This part of the project now represents the bulk of the work and, as such, this quarterly report is largely reporting on work leading to this outcome.*

SEISta Milestones FY18: Silicon Electrolyte Interface Stabilization (SEISta)

SEISta Team

Background

The overall objective of the SEISta project is to better understand the formation and evolution of the solid-electrolyte interphase (SEI) on silicon anodes. Silicon is a viable alternative to graphitic carbon as an electrode in lithium-ion cells and can theoretically store >3,500 mAh/g. However, lifetime problems have been observed that severely limit its use in practical systems. The major issues appear to involve the stability of the electrolyte and the uncertainty associated with the formation of a stable SEI at the electrode. Recently, calendar-life studies have indicated that the SEI may not be stable even under conditions where the cell is supposedly static. Clearly, a more foundational understanding of the nature of the silicon/electrolyte interface is required if we are to solve these complex stability issues. A multi-lab consortium has been formed to address a critical barrier in implementing a new class of materials used in lithium-ion batteries that will allow for smaller, cheaper, and better performing batteries for electric-drive vehicles. This consortium—the Silicon Electrolyte Interface Stabilization (SEISta) project—was formed to focus on overcoming the barrier to using such anode materials. Five national laboratories, led by the National Renewable Energy Laboratory (NREL), are involved: NREL, as well as Argonne (ANL), Lawrence Berkeley (LBNL), Oak Ridge (ORNL), and Sandia National Laboratories (SNL).

Quarter 1 Milestone:
Have determined if the pristine surface of the silicon influences the composition and the function of the SEI after 1, 10 and 50 cycles (XPS, SIMS, IR, and Raman, STEM, SSRM).

Results

For FY18, all milestones are 100% complete. Most of the following report details the work that enables the completion of this milestone. Specific finding from this work are that the non-passivating behavior of silicon thin films has been directly observed for the first time as an independent effect from the cracking of silicon particles due to the lithiation. In addition dense thermal oxides of 5 nm or more severely impede lithiation, whereas 1 nm SiO_2 allows lithiation to proceed unimpeded. However, SEIs formed on native SiO_x on Si were thicker, as determined by XPS and SSRM. XPS results showed that SEI formed on native SiO_x showed greater C, Li, and F content. Clearly the nature of the silicon surface is major factor in the stabilization of the SEI. We will explore this more in the coming months.

Examination of the Passivating Nature of the Silicon Electrolyte Interface (SEISta) [LBNL]

Joint report LBNL (I. Hasa, L. Zhang, P. Ross, R. Kostecki) and ORNL (G. Yang, G. Veith)

Background

The primary objective of our effort is to clarify and understand the processes occurring at the silicon/electrolyte interface. The reductive decomposition of the electrolyte in lithium-ion systems employing silicon anodes is inevitable, since the working potential of the electrode is far below the electrochemical stability window of the electrolyte components. In principle, the insoluble decomposition products precipitating on the electrode surface, result into the formation of a passivating surface film which suppress further electrolyte decomposition.[1,2] However, the inherent instability of the silicon/electrolyte interface strongly inhibits the surface passivation, which is further endangered by the mechanical instability of the electrodes, which upon alloying with lithium experience a huge volume expansion responsible of active material cracking and consequent instability of the passivating film.[3] A better understanding of the kinetic processes occurring upon cycling will enable an efficient implementation of silicon based electrodes in high performance lithium-ion batteries. To accomplish this, we address the inherent non-passivating behavior of silicon model electrodes in organic electrolytes. In particular, this last quarter we have been focused on the "Corrosion Task" of the SEISta project, which is a coordinated research thrust aiming at the understanding and the evaluation of the non-passivating behavior of silicon anodes. The overall goal of this effort is to provide a basic understanding and ways of effective mitigation of Si anode corrosion in organic carbonate-based electrolytes. Oak Ridge National Laboratory fabricated all the model electrodes for the Corrosion task, while the team at Berkeley Lab electrochemically investigated the corrosion currents involved upon cycling.

Results

The evaluation of the passivating properties of silicon anodes involved the definition of the electrochemical protocols to be employed for the determination of the corrosion currents. Two different electrochemical protocols have been established involving galvanostatic tests followed by chronoamperometry measurements, both in potentiostatic mode at fixed voltage values (Protocol 1), and at open circuit voltage conditions (Protocol 2). A schematic of the electrochemical cell and a description of the two protocols is given in Fig.1.
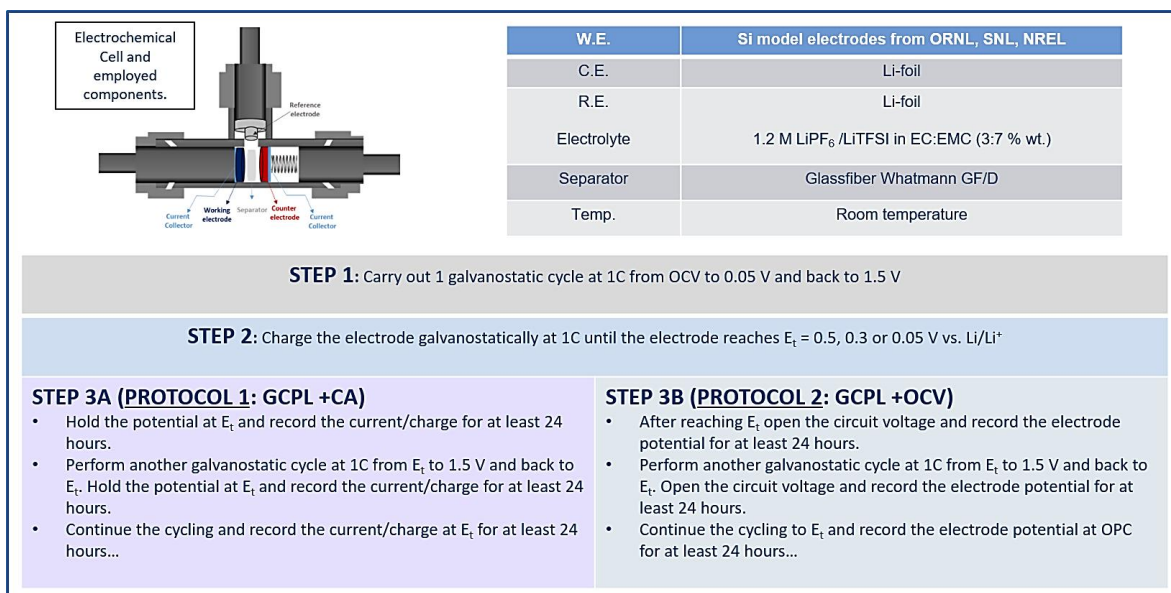

W.E.	Si model electrodes from ORNL, SNL, NREL
C.E.	Li-foil
R.E.	Li-foil
Electrolyte	1.2 M LiPF$_6$ /LiTFSI in EC:EMC (3:7 % wt.)
Separator	Glassfiber Whatmann GF/D
Temp.	Room temperature

STEP 1: Carry out 1 galvanostatic cycle at 1C from OCV to 0.05 V and back to 1.5 V

STEP 2: Charge the electrode galvanostatically at 1C until the electrode reaches E$_t$ = 0.5, 0.3 or 0.05 V vs. Li/Li$^+$

STEP 3A (PROTOCOL 1: GCPL +CA)
- Hold the potential at E$_t$ and record the current/charge for at least 24 hours.
- Perform another galvanostatic cycle at 1C from E$_t$ to 1.5 V and back to E$_t$. Hold the potential at E$_t$ and record the current/charge for at least 24 hours.
- Continue the cycling and record the current/charge at E$_t$ for at least 24 hours…

STEP 3B (PROTOCOL 2: GCPL +OCV)
- After reaching E$_t$ open the circuit voltage and record the electrode potential for at least 24 hours.
- Perform another galvanostatic cycle at 1C from E$_t$ to 1.5 V and back to E$_t$. Open the circuit voltage and record the electrode potential for at least 24 hours.
- Continue the cycling to E$_t$ and record the electrode potential at OPC for at least 24 hours…

Figure 1. Schematic representation of the electrochemical cell set up, cell components and protocols employed in the Corrosion Task.

Following the definition of the protocols, a screening study of the most suitable model electrodes has been performed. The selection criteria for the determination of the best model electrodes involved the quantification of the residual currents (corrosion currents) upon cycling. A fundamental requirement for the substrates is that lithiation should occur exclusively at the expense of the amorphous silicon thin film deposited on the substrates, so that the latter ones should result inert toward lithiation and should present a very smooth and defined surface for the deposition of amorphous silicon.

Figure 2 shows representative images of some of the electrode prepared for this work. We chose copper based current collectors due to its stability against lithium metal. The choice of electrode materials can be divided into two classes of electrodes: (1) copper encapsulated substrates and (2) pure metal rods. The encapsulated substrates were prepared by sectioning silicon or sapphire wafers. These wafers coated on the "rough" side by physical vapor deposition from a high purity copper target. A 20 µm film was deposited on the substrate back and rained down along the sides. The substrate was flipped and an additional 2 µm of Cu was deposited on the "smooth" side of the substrate. Electrical continuity was measured on each substrate to estimate if copper coated the entire substrate. A portion of the copper coated substrates were loaded on a substrate holder and a silicon film was deposited on the "smooth" side of the substrate (Fig. 2- Right).

The second set of samples were prepared using high purity oxygen-free high thermal conductivity (OFHC) copper. 3" rods of copper along with 2 mm disks of cupper were cut from OFHC rod stock. The diameter of the rod was set to fit the Swagelok cells used for the corrosion current tests. The cut rods and disks were polished with progressively finer grits (down to 0.3 µm) until a mirror like finish was obtained, Fig. 2 – Middle. The rods were cleaned in hexane to remove oils and a dilute citric acid to remove residual oxide and polar molecules. Some rods were coated with PVD shrink wrap (McMaster Carr) to attempt to further isolate the sides of the rods from electrochemical reactions. 50 nm amorphous silicon films were deposited on the polished copper rods using the same chamber and deposition conditions, Fig. 2 - Left. The sides of the rods were masked with Kapton tape to produce a well-defined electrode area.
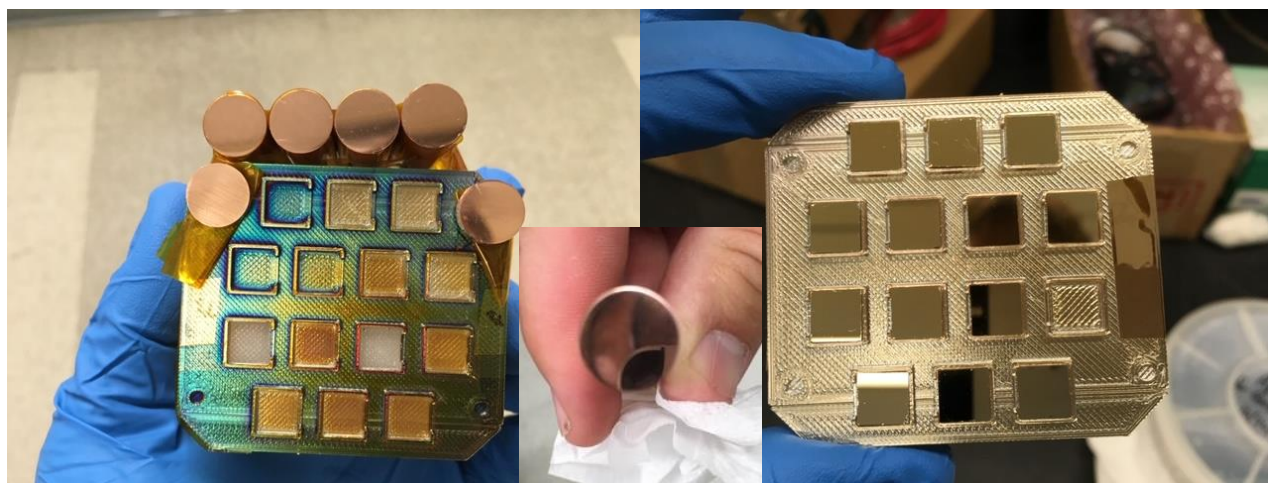

Figure 2. *Left – Images of copper rods before silicon deposition; Middle – image of polished copper rod surface; Right – Picture of as grown silicon films on copper coated sapphire.*

Figure 3 shows schematic cross sections of the electrodes (top) along with representative cyclic voltammetry data collected for the bare and silicon coated substrates. These encapsulated model electrodes exhibited large currents and allowed partial lithatiation. As a result, these samples were discontinued due to lithiation of the substarate underneath the copper film. The copper piston was identified as the best substrate due to its (expected) inactivity toward lithium.
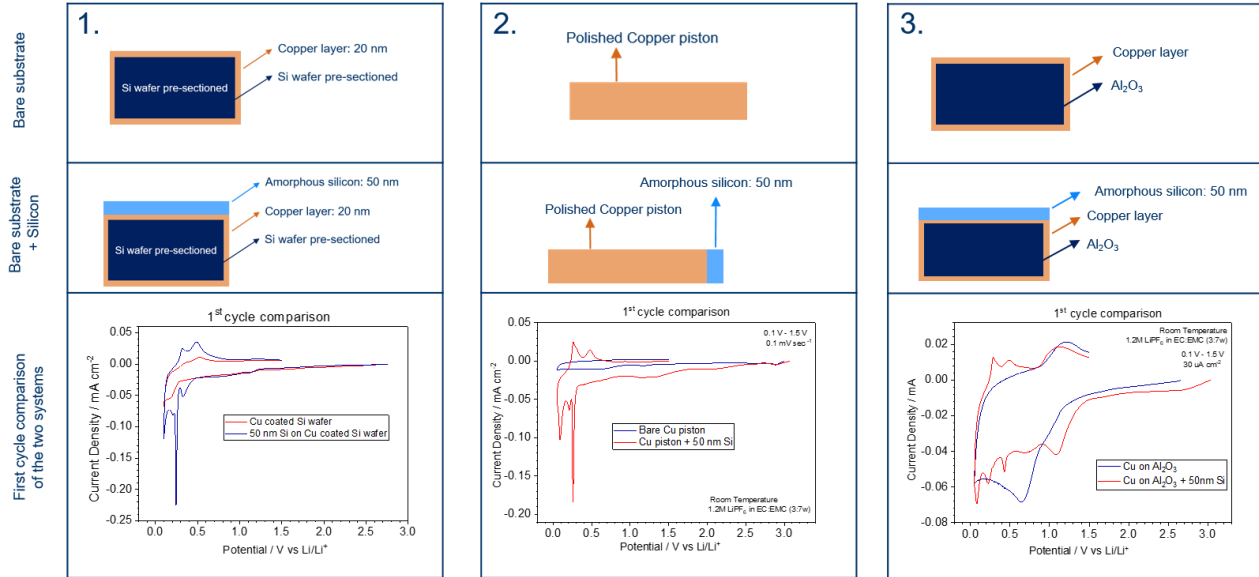

Figure 3. Schematic of the three model electrodes investigated to evaluate the inactivity of the substrates. Comparative cyclic voltammetry tests (1st cycle shown) for the bare substrates and the substrates with the sputtered amorphous silicon. Tests performed at room temperature using Gen 2 electrolyte (1.2 M LiPF$_6$ in EC:EMC 3:7 % wt.).

The developed Protocol 1 (GCPL +CA) has been applied to the selected model electrode and the residual currents after every lithiation have been calculated and reported in Fig. 4.
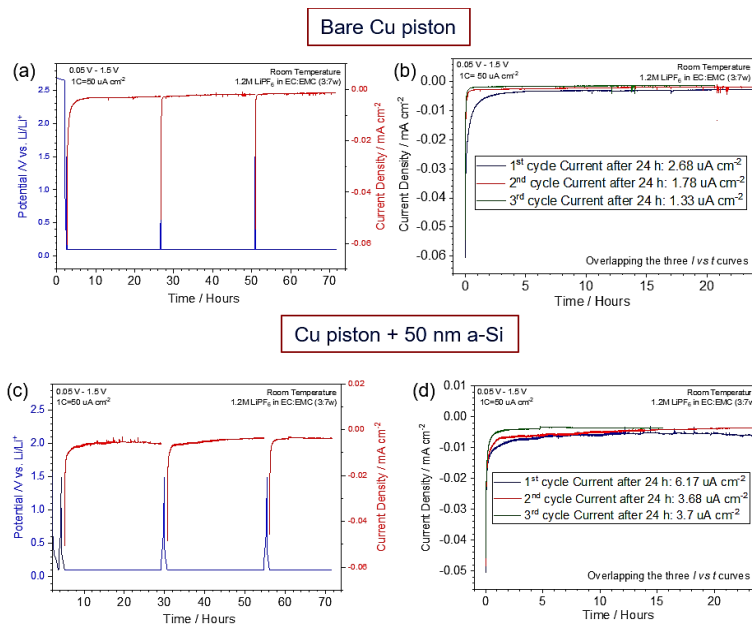
Figure 4. Application of Protocol 1 (GCPL +CA) to the bare copper substrate (a, b) and to the silicon added model electrode (c, d). Fig. (a) and (c) show the first galvanostatic cycle at 50 µA cm^{-2} and the second lithiation followed by a potentiostatic voltage step for 24 hours at 0.05 V. The test has been applied for three cycles. The current change during the 24 hours has been monitored and plotted as overlapping I vs t curves in Fig. (b) and (d). Tests performed at room temperature using Gen 2 electrolyte (1.2 M LiPF$_6$ in EC:EMC 3:7 % wt.).

Fig. 4 shows that the residual background current value observed after the 1st cycle is about 2.7 µA cm^{-2} for the bare copper piston, while by adding silicon, the residual current is about 6.1 µA cm^{-2}. The results indicate that almost one third of the current values observed is associated to the copper

piston. The current values involved with the bare Cu substrate are very large and most likely related to the large surface area of copper exposed to the electrolyte in T-cell configuration. In order to find a more suitable substrate involving less exposed surface area, different copper substrates have been tested. A schematic representation of the investigated substrates and the residual current values observed after the 1st cycle by appling Protocol 1 are reported in Table 1.
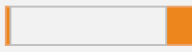
Substrate	Cu piston	Cu piston + protective plastic	Cu thick disk	Cu foil
Residual Current after 1st cycle	2.7 µA cm^{-2}	1.8 µA cm^{-2}	2.6 µA cm^{-2}	1.0 µA cm^{-2}

Table 1. *Copper based substrates investigated with Protocol 1. The values of the residual current observed after 24 hours of potentiostatic step at 0.05 V are reported. The thin copper foil presents the lower values of the order of 1 µA cm^{-2}.*

Copper foil (12 mm diameter) presented the smaller residual current values. Accordingly the first model electrode of choice for the evaluation of the corrosion currents has been identified as : 500 nm amorphous silicon (with 3 nm native oxide) deposited on copper foil (500 nm Si + 3 nm SiO$_2$ on Cu). The 500 nm Si thin film has been investigated in four electrolyte solutions, *i.e.* 1.2 M LiPF$_6$ EC:EMC (3:7 wt%), 1.2 M LiPF$_6$ EC:EMC (3:7 wt%) + 10%wt. FEC, 1.2 M LiTFSI EC:EMC (3:7 wt%) and 1.2 M LiTFSI EC:EMC (3:7 wt%) + 10%wt. FEC. The electrochemical characterization has been performed both in terms of cyclic voltammetry and galvanostatic cycling test as reported in Fig. 5.
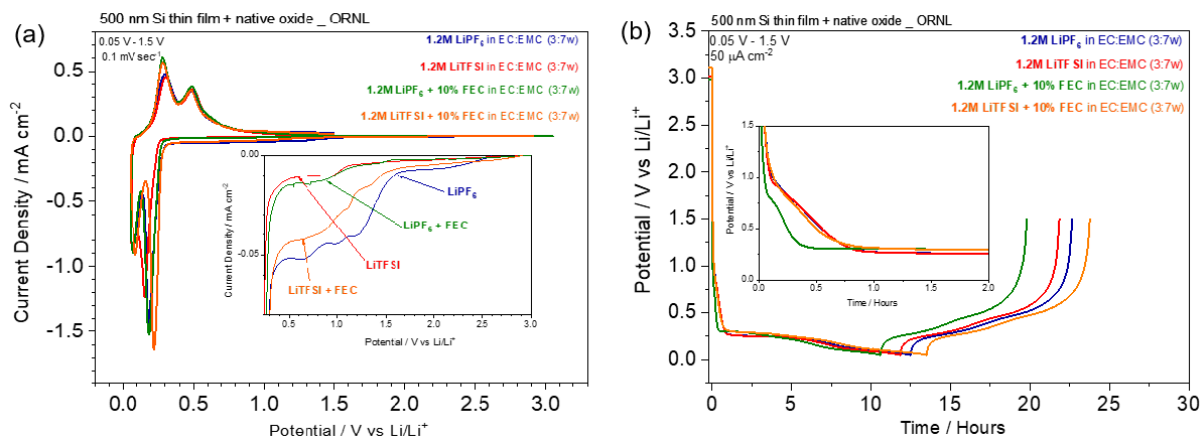

Figure 5. *(a) First lithiation –de-lithiation process of 500 nm Si thin film on Cu foil observed by cyclic voltammetry by using four different electrolyte solutions. A scan rate of 0.1 mV sec^{-1} has been applied within the 0.05 V – 1.5 V potential range. Inset shows the enlarged potential region of the electrolyte decomposition. (b) Galvanostatic cycling test of the same systems performed at 50 µA cm^{-2}.*

Interestingly, the inset of Fig. 4 reports the current values involved during the electrolyte decomposition process occurring before lithiation. The LiPF$_6$ based electrolyte presents the largest reductive current density, while the presence of FEC and the substitution of LiPF$_6$ with LiTFSI strongly reduce the current involved in the process. The observation has been confirmed by galvanostatic cycling test as reported in Fig. 4 (b). Indeed, the first Coulombic efficiency has been calculated to be: 81.4%, 84.3%, 86.5% and 75.8% respectively for the 1.2 M LiPF$_6$ EC:EMC (3:7 wt%), 1.2 M LiPF$_6$ EC:EMC (3:7 wt%) + 10% FEC, 1.2 M LiTFSI EC:EMC (3:7 wt%) a0nd 1.2 M LiTFSI EC:EMC (3:7 wt%) + 10% FEC electrolyte solutions. Protocol 1 (GCPL + CA) has been applied to the above-mentioned system in order to understand and evaluate the effect of different salts

(LiPF$_6$ vs LiTFSI) and the effect of the additive addition (10% wt. FEC) on the passivating properties of silicon.

Fig. 6 reports the galvanostatic cycling test (with associated potentiostatic steps) and the *I vs t* curves obtained during the constant voltage step at 0.05 V for the 500 nm Si thin film in three different electrolytes.
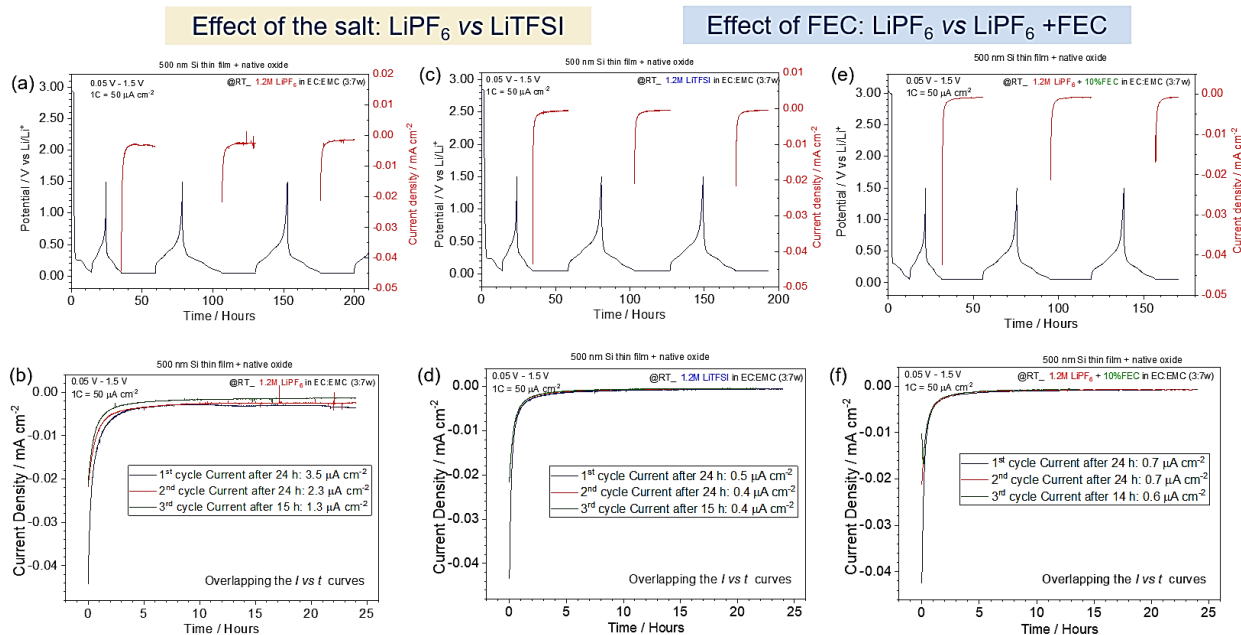

Figure 6. Application of Protocol 1 (GCPL +CA) to the 500 nm Si thin film model electrode by using (a, b) 1.2 M LiPF$_6$ EC:EMC (3:7 wt%), (c, d) 1.2 M LiPF$_6$ EC:EMC (3:7 wt%) + 10% FEC, and (e, f) 1.2 M LiTFSI EC:EMC (3:7 wt%). (a, b, c) show the galvanostatic cycling with associated potentiostatic step at 0.05 V. (b, d, f) reports the related current density measurement during the potentiostatic step.

It is interestingly shown that the residual current detected after 24 hours at 0.05 V are very large for the 1.2 M LiPF$_6$ EC:EMC (3:7 wt%) electrolyte, while by substituting LiPF$_6$ with LiTFSI, the current value is about 7 times smaller. The same effect is observed with the addition of 10 % FEC to the bare 1.2 M LiPF$_6$ EC:EMC (3:7 wt%) solution. The data are in agreement with the CV and GCPL tests reported in Fig.5. It is also observed that the passivation of silicon improves upon cycling, as demonstrated by the lower current values observed after the third potentiostatic step when compared to the first one.

The same kind of analysis has been conducted to investigate also other effects on the corrosion currents and passivating properties of silicon. The investigated effects include: the state of charge at which the potentiostatic step is applied (0.5 V *vs* 0.05 V), the effect of the silicon thickness (500 nm Si *vs* 50 nm Si - cracking effect of silicon upon cycling-), and the effect of the surface silicon oxide layer on silicon which has also been investigated by applying protocol 2 (GCPL +OCV) (3 nm native SiO$_2$ *vs* 10 nm sputtered SiO$_2$).

All the investigated effects and related preliminary conclusions are summarized below in Table 2.

Table 2. Summary of the investigated effects on the passivating properties of silicon and preliminary conclusions.

INVESTIGATED EFFECTS	CONCLUSION
Effect of the salt : LiPF$_6$ vs LiTFSI:	LiTFSI based electrolytes exhibit lower residual currents
Effect of additives: 10% wt. FEC addition	FEC improves the passivation properties of Si
Effect of the state of charge on corrosion current: 0.5 V vs 0.05 V	Larger currents are observed at 0.05 V than 0.5 V.
Effect of Silicon thickness: 500 nm vs 50 nm Si decoupling cracking effect from catalytic activity of Si	The cracking effect is responsible of about 60 % of the parasitic currents observed in fully lithiated state
Effect of SiO$_2$ on passivating behavior	SiO$_2$ inhibits passivation of silicon surface

Conclusions

The corrosion task has led to the definition of standard protocols enabling a relative quantification of the non-passivating behavior of silicon model electrodes. A set of electrodes has been investigated to define the model electrodes of choice. Silicon thin films have been identified as the best model electrodes so far investigated. By applying Protocol 1 and 2 to various systems characterized by different properties (thickness of silicon, thickness of the oxide surface layer) and also different interfaces (employment of four types of electrolyte solutions) preliminary conclusions have been obtained.

In summary, the non-passivating behavior of silicon thin films has been directly observed for the first time as an independent effect from the cracking of silicon particles due to the lithiation. A visualization of the improvement of the passivation properties upon cycling has been quantified, suggesting a thickening of the passivating film on the silicon surface. The beneficial effect of FEC for the SEI stability has been confirmed and the use of LiTFSI as alternative salt to improve the SEI stability is proposed. According to our preliminary results, the silicon oxide layer has a detrimental effect on the passivating properties of silicon electrodes. Further studies in this regard are still required.

References

[1] E. Peled, *J. Electrochem. Soc.*, **126**, 2047-2051 (1979).
[2] M. Winter, *Zeitschrift Für Phys. Chemie*., **223**, 1395-1406 (2009).
[3] M.N. Obrovac, V.L. Chevrier, *Chem. Rev*., **114**, 11444-11502 (2014).

Nature of the Silicon Surface with Cycles – *in-situ* Spectroscopic Analysis (NREL)

Sang-Don Han and Bertrand Tremolet de Villers (NREL)

Background

Due to complexity, high reactivity and continuous evolution of a silicon-electrolyte interphase (SiEI), it remains a poorly understood topic in advanced Li-ion battery research and its detailed and real-time analysis is a great challenge. Vibrational spectroscopy is one of the most important avenues for understanding and quantifying the interfacial chemical and electrochemical reactions. Raman and Infrared (IR) spectroscopy are attractive due to their versatility, and they are used extensively by the battery community in their *ex-situ* form. Developing *in-situ* methods of these techniques, however, will provide new insight and help in elucidating the mechanism of interfacial failure in battery systems. Moreover, combining *in-situ* analysis from both Raman and IR spectroscopy will provide detailed and complementary information. Raman spectroscopy relies on polarizing the electron cloud associated with a chemical bond, rather than measuring the associated dipole moment (as in IR spectroscopy). Therefore, the combination of these two techniques in one study enables analysis that may otherwise be missed by applying only a single technique. This study can provide a guidance to stabilize SiEI by understanding of the underlying chemistry and physics and providing mechanical explanation of surface chemistry and various reactions/interactions within the SiEI.

Results

The demonstrated experiment has the unique ability to link the causal nature of the electrochemical response with both the changing solution structure of the electrolyte and the evolving SiEI. In doing so, it can provide a mechanistic insight into the origins of deleterious performance in Si anode systems. This work aims to remedy the void in understanding how reduction of electrolyte (upon discharge) and (de)insertion of Li^+ ions into Si anode (upon discharge/charge) effects Si anode-electrolyte interface. Specifically, the Raman analysis can be paired with electrochemical analytical techniques—such as cyclic voltammetry and chronopotentiometry/chronopotentiometry—to determine which solution structures and/or aspects of the electrolyte decompose at specific voltages and cycles and how these changes influence on Si anode-electrolyte interphase. This analysis will help inform the rational design of next generation electrolyte systems including additives designed for Si-based advanced battery systems.

In-situ Raman Cell and Instrumentation Details. Based on extensive literature and internet survey an *in-situ* Raman cell (Fig. 1, ECC-Opto-Std) was purchased from EL-CELL GmbH to investigate the electrode-electrolyte interface before, during and after electrochemical operation.[1] Among four different cell configurations (e.g., 2-electrode sandwich, 2-electrode side-by-side, 3-electrode side-by-side, and standard sandwich) 2-electrode side-by-side setup (left picture of Fig. 1) was selected to enable focusing electrode-electrolyte interface during cycling. The cell is expected to measure solution structure and chemical composition and to analyze (electro) chemical reactivity and evolution.

Figure 1. *in-situ* cell with side-by-side setup for spectroscopic analysis.

We are using a Renishaw inVia confocal Raman microscope with three available laser light excitation choices: 532 nm, 633 nm, and 785 nm. So far, we have only used the 532 nm source as it seems to provide the best signal from our samples with minimal fluorescence background. The 50x metallurgic microscope lens (0.9 NA) combines good confocality and light collection. The sapphire (Al_2O_3) window of the *in-situ* cell holder is thin enough (300 µm) to allow a focal spot on the silicon wafer and electrolyte below the window.

Initial measurements and peak assignments. Fig. 2 shows a typical Raman spectrum collected through an *in-situ* cell holder. We have invested time to build a reference table for peak assignments (Table 1), and continue to refine it. Fig. 3 shows the Raman spectra for both electrolyte systems: Gen2 electrolyte *vs.* Gen2 with 10 wt% FEC electrolyte. Based on a comparison of the two electrolyte systems, Raman shift of FEC (e.g., 728, 868, and 908 cm^{-1}) can be assigned as shown in Table 1.
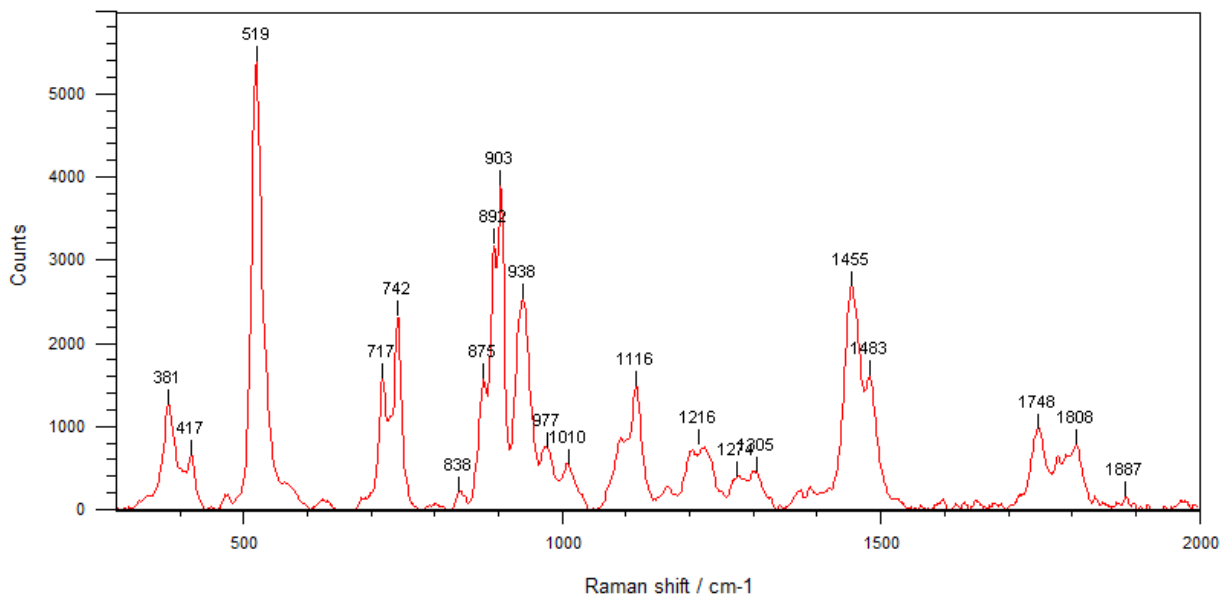
Figure 2. Representative Raman spectrum with an *in-situ* cell. Observed peaks were assigned to the sapphire window (381, 417, 748 cm^{-1}), a strong signal from the crystalline silicon wafer anode (520 cm^{-1}), and many peaks assigned to the various components of a standard Gen2 electrolyte (1.2M LiPF$_6$ in 3:7 EC:EMC).
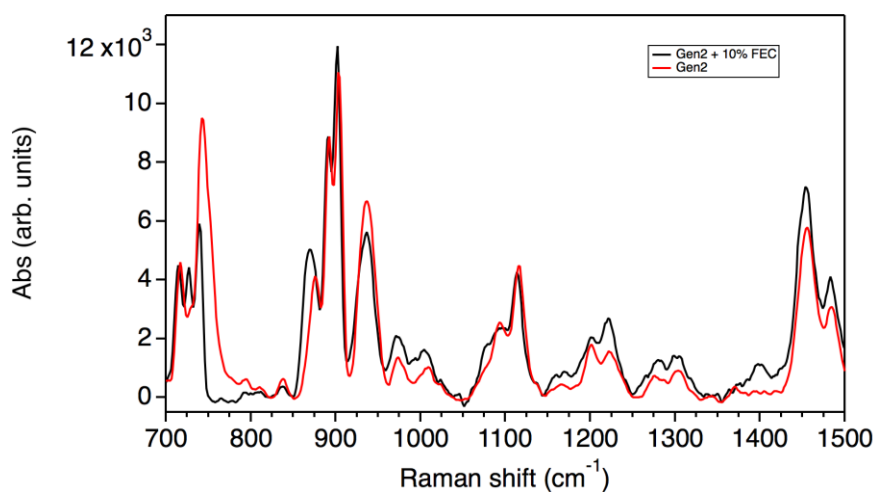

Figure 3. Comparison of Raman spectra of Gen2 electrolyte (red) and Gen2 with 10% wt. FEC additive (black).

Table-1: Raman peak assignments

Raman Band Center (cm^{-1})	Assignment	Species of Origin	Reference(s):
380	E_g	Al_2O_3	1
417	A_{1g}	Al_2O_3	1
431	E_g	Al_2O_3	1
450	E_g	Al_2O_3	1
480		a-Si	
513		?	
520	1TO	c-Si	
530		?	
578	E_g	Al_2O_3	1
645	A_{1g}	Al_2O_3	1
720	o, O-C-O	EC	2
728	o, O-C-O	FEC	2
733	o, O-C-O	EC$\cdots$Li$^+$	2
740	υ, P-F	PF$_6^-$	2
742	υ, P-F	PF$_6^-\cdots$Li$^+$	2
748	E_g	Al_2O_3	1
868	υ, C-F	FEC	2
897	β, C-C	EC	2
908	β, C-C	FEC	2
932	δ, O-C-O	EMC	3, this work
945	δ, O-C-O	EMC$\cdots$Li$^+$	3, this work
1488	δ, CH$_3$	EC	2
1705-1730	υ, C=O	EMC$\cdots$Li$^+$	this work
1748	υ, C=O	EMC	this work
1778	υ, C=O	EC	2
1804	υ, C=O	EC	2

References: (1) DOI:10.1063/1.367972, (2) DOI:10.1021/acsnano.8b05038, (3) DOI:10.1039/C6CP07215A

Preliminary in-situ Raman Measurements upon Cycling. For *in-situ* Raman measurement, a crystalline silicon wafer (c-Si, 525 μm, <0.005 Ω cm, p-type) strip and a lithium metal foil were used as the working and the counter/reference electrodes, respectively (Fig. 1). Raman spectra was collected at various voltages/times during galvanostatic cycling (at 5 μA) of the *in-situ* cell. The OCV of assembled cell was at around 2.85 V *vs.* Li/Li$^+$ (hereafter), which is usually observed from coin-type cell cycling tests (Fig 4). Upon the 1st discharge (2.85 - 0.11 V) electrolyte decomposition and initial SiEI formation were observed at between ~1.3 and 0.11 V (left side of red-dotted line). Then, lithiation of c-Si (c-Si + xLi → a-Li$_x$Si) was observed at around 0.115 V for 14 hrs as programmed. Upon the 1st charge (0.11 - 1.50 V) low-voltage and high-voltage delithiation plateaus of amorphous Si were observed as shown in previous study:[2] a-Li$_{(x'+x'')}$Si → a-Li$_x$Si + x''Li and a-Li$_x$Si → a-Si + x'Li. In the case of Raman spectra during discharging and charging, we observed a reduction of the crystalline silicon peak at 520 cm^{-1} and an increase in a broad feature that may be amorphous silicon (broad, centered ~480 cm^{-1}) as shown in Fig 4 (inset).
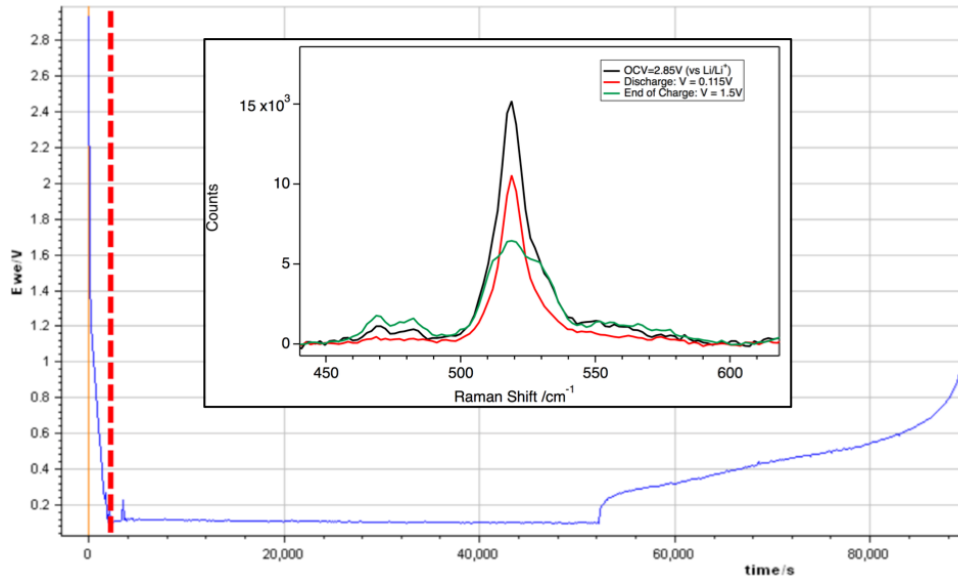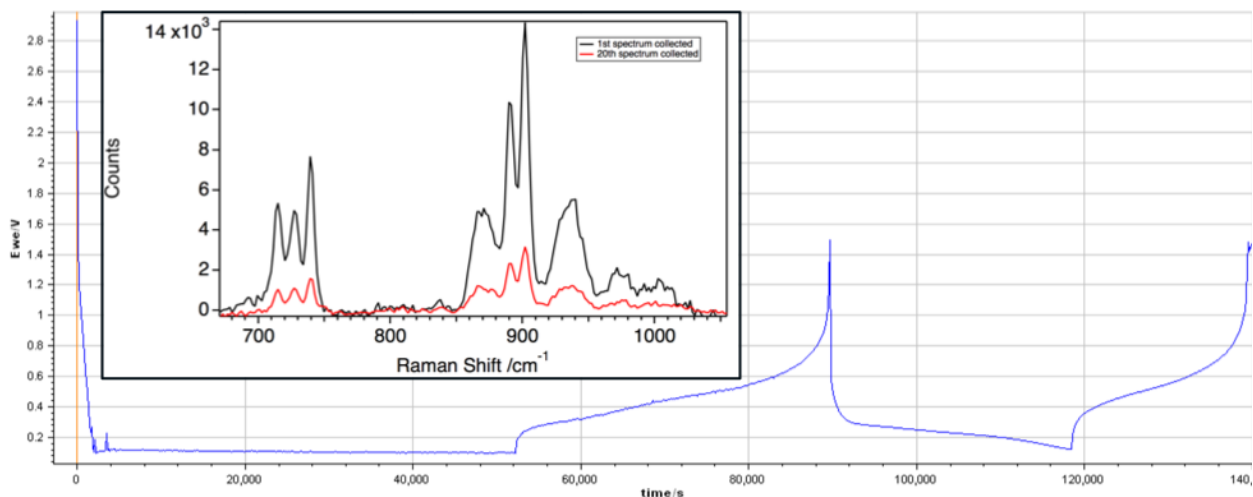
Figure 4. Galvanostatic cycling of the *in-situ* Raman cell and Raman spectra collected during the first cycle (inset).

Problems encountered and mitigating strategies. We are still exploring optimal measurement parameters, such as light excitation intensity, collection time, spectra averaging, and objective height, because of weak S/N ratios for some important electrolyte component scattering bands, e.g., EMC coordinated with Li+ in the region of 1700 - 1740 cm⁻¹. To increase our signals, we are trying different combinations of light excitation intensity (1- 50 mW), collection time (2 - 300 sec), and spectra averaging (3 - 50 accumulations). Increasing the excitation intensity certainly increases the S/N ratio, but can easily damage the samples. Fig. 5 shows Raman spectra collected at the same spot at 50 mW 532 nm laser excitation. Initially, we have good S/N, but after 20 collected spectra, we see that we have lost most of our signal. Subsequently, we have lowered the excitation intensity and increased the collection time from 10 sec to 300 sec. If we have to wait 5 mins for one spectrum, we may miss some of the dynamics happening during the cell electrochemical cycling.

Figure 5. Galvanostatic cycling of the *in-situ* Raman cell and Raman spectra collected during the first cycle (inset).

In addition, we are struggling to find an appropriate spot for SiEI study (right above the Si wafer *vs.* side of the Si wafer) because of inhomogeneous distribution of SiEI in an overall Si wafer strip, which is possibly due to heterogeneous structure of each material and consequences lack of electrolyte (and limited Li+ ion

14

conductivity). Therefore, we're designing a different shape of Si wafer to obtain relatively homogeneous distribution of SiEI, which can facilitate *in-situ* Raman measurements.

Conclusions

Based on extensive literature survey and several initial Raman measurements, we built a reference table for peak assignments of standard Gen2 electrolyte components (e.g., EC, EMC, PF_6^-), additive (FEC), and an *in-situ* cell part (e.g., Al_2O_3), which continues to refine. Utilizing a well-designed *in-situ* cell a reasonable and meaningful electrochemical performance data was obtained with initial promising Raman data. We'll address the issues that we encountered during preliminary *in-situ* Raman measurements by exploring optimal measurement parameters, designing a different shape of Si wafer, and finding an appropriate Raman measurement spot.

References

1. https://el-cell.com/
2. M. N. Obrovac and L. J. Krause *J. Electrochem. Soc.* **2007**, *154*, A103-A108.

Electrochemical Testing of Silicon Wafer Anodes With SiO$_2$ Coatings (NREL)

Manuel Schnabel (NREL), Steve Robbins (NREL), Chunmei Ban (NREL), Paul Stradins (NREL)

Background

Polished silicon wafers provide the most controlled silicon material with which to study the fundamental processes occurring during the lithiation of silicon from an electrolyte. In addition, they can be oxidized, resulting in dense SiO_2 layers of varying thickness whose effect on lithiation and battery electrochemistry can be studied as a model system for – typically oxidized – Si powders that would be used in commercially relevant batteries. In the following, we describe results obtained on Si wafer anodes with 1-30 nm SiO_2 coatings. The coatings were prepared by thinning 100 nm thermally grown SiO_2 on Si down to the desired thickness using a buffered HF etching process developed in FY18.

Results

1. O-ring Cells for Accurate Electrochemical Characterization – Achieving reproducibility

As reported in FY18, Si wafers with SiO_2 coatings must be tested in cells that define the electrochemically active area of the wafer using an O-ring in order to avoid participation of the wafer edges or rear in the electrochemical processes. This is crucial because the edges in particular are not coated with SiO_2 and are thus initially much more electronically conductive.

However, a cell with an O-ring necessarily utilizes a larger electrolyte volume, and we found that this can lead to more pronounced side reactions. When only cleaning cell parts in dimethyl carbonate between experiments, galvanostatic cycling at $20\mu Acm^{-2}$ yields continuous electrolyte reduction at voltages far above the lithiation potential. Through a series of experiments, it was found that using fresh Li metal for reference and counter electrodes, using fresh electrolyte, and cleaning cell parts in organic solvents as well as water between experiments, was crucial to suppress electrolyte reduction. With this procedure, we are able to achieve lithiation at current densities down to $5\mu Acm^{-2}$. Unfortunately, current densities of 2.0 and $0.7\mu Acm^{-2}$ do not allow lithiation even with this optimized procedure (see Fig. 1). This result agrees with one reported by LBL earlier, suggesting that this effect is not related to our particular cell components, but perhaps to the fact that ~1.4mL electrolyte is used per cm^2 of anode area, as opposed to $\sim20\mu Lcm^{-2}$ in a typical coin cell.
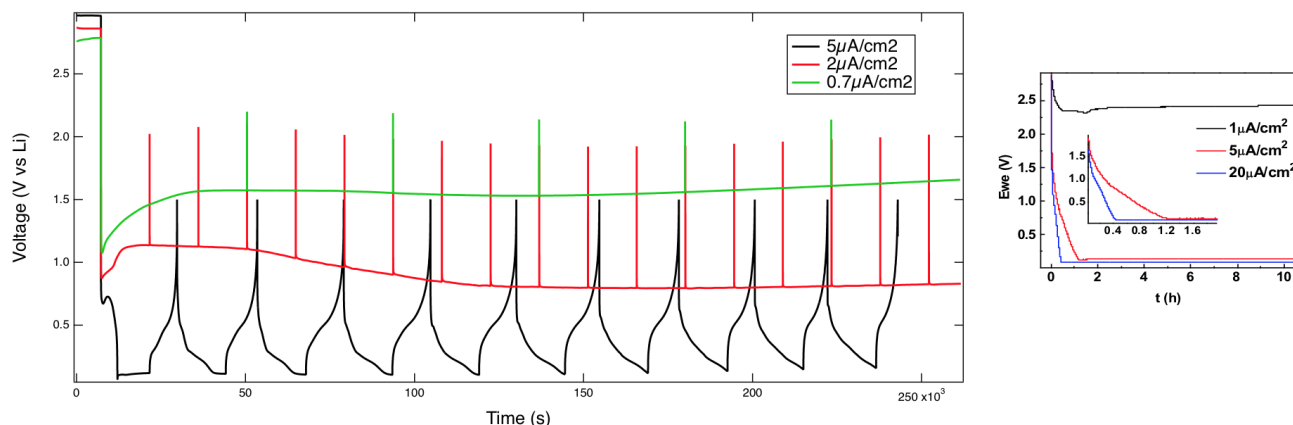
Figure 1. Galvanostatic cycling results obtained with an O-ring cell and Si wafer anode as a function of current density at NREL (4h half-cycles for 5 and 2µAcm^{-2} , 12h for 0.7µAcm^{-2}) . Right: comparable results reported by LBL for a single lithiation cycle.

2. Effect of SiO$_2$ thickness on lithiation

Utilizing these O-ring cells, we proceeded to study the effect of 1-30 nm thermal SiO$_2$ coatings on the lithiation of Si wafers. Galvanostatic cycling at 20 µAcm^{-2} in Gen2 electrolyte indicates that while Si with 1 nm SiO$_2$ will lithiate above 0 V vs Li, Si with 3 nm SiO$_2$ will only lithiate after a potential spike to -0.4V vs Li. Thereafter, it actually cycles with higher Coulombic efficiency (CE) than Si with 1 nm SiO$_2$. However, Si with 5-30 nm SiO$_2$ initially require voltages below -1.0V vs Li to sustain 20 µAcm^{-2}, resulting in localized Li plating at pinholes in the SiO$_2$ rather than lithiation. The latter is confirmed by visual inspection of the electrodes after cycling, and is also evident from the Coulombic efficiencies, which exceed 98% after the first
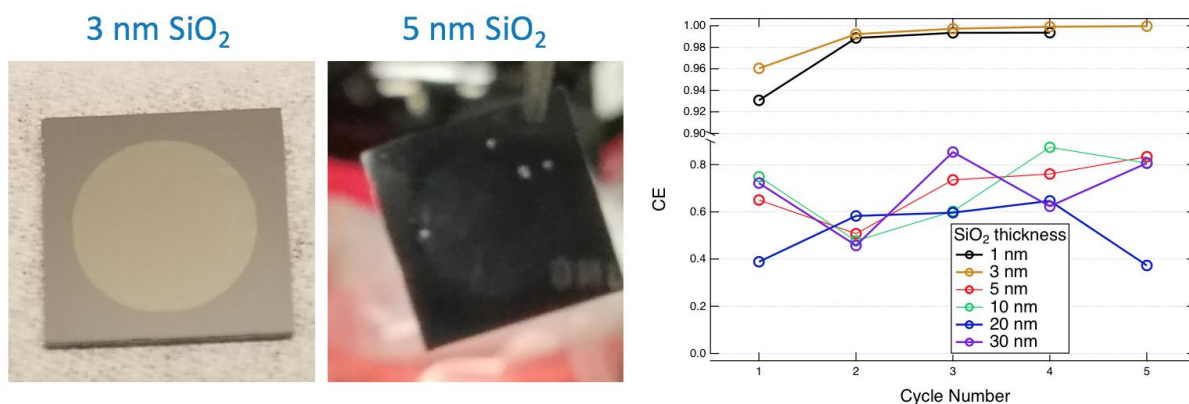
cycle for 1 and 3 nm SiO$_2$ but vary wildly between 40 and 85% for 5nm or more of SiO$_2$ (see Fig. 2).

Figure 2. Photographs of Si wafers with 3 nm (left) and 5 nm (middle) after galvanostatic cycling at 20µAcm^{-2} without lower potential cutoff. The former lithiates in area defined by O-ring, whereas latter does not lithiated and undergoes Li plating and stripping at pinholes. Right: Coulombic efficiency (CE) of galvanostatic cycling for different SiO$_2$ thicknesses. 3 nm SiO$_2$ yields higher CE than 1 nm SiO$_2$. 5 nm SiO$_2$ and above have terrible CE as only Li pinhole plating and stripping occurs.
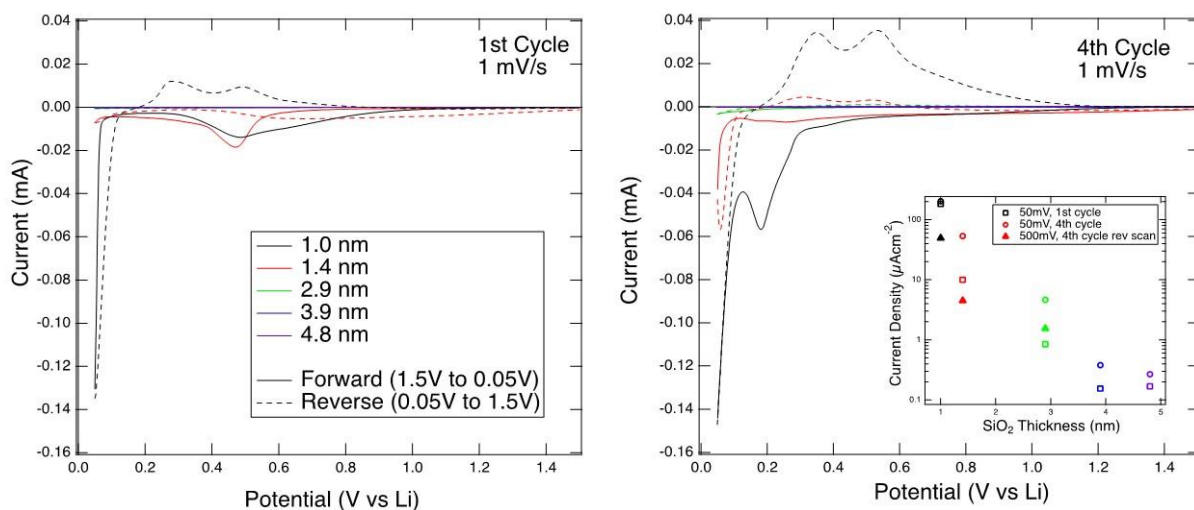
Figure 3. Cyclic voltammetry curves (left_ 1st cycle, right: 4th cycle) obtained on Si wafers with 1-5 nm SiO₂. Inset: peak currents as a function of SiO₂ thickness.

To understand these phenomena in more detail, cyclic voltammetry (CV) was performed on Si with 1-5 nm SiO₂ (see Fig. 3). Lithiation only occurred in the 1.0 nm sample in the first cycle, but by the fourth cycle, lithiation occurred in samples with up to 2.9 nm SiO₂. Samples with 3.9 nm and 4.6 nm SiO₂ on the other hand exhibit no lithiation or reversible electrochemistry during ten CV cycles. Two distinct delithiation peaks are observed for 1.0 and 1.4 nm SiO₂, but only the higher-voltage peak is observed for the 2.9 nm SiO₂, suggesting a unique delithiation chemistry that may be correlated to the high CE during galvanostatic cycling. The peak currents (0.05mV for lithiation, 0.5V for delithiation) decrease exponentially with SiO₂ thickness, indicating that tunneling electron transfer across the SiO₂ may play a key role in the reaction kinetics.

Conclusions

We have developed a way to reliably cycle coated Si wafers in a manner free from edge effects at current densities down to $5\mu Acm^{-2}$. Applying this technique to studying Si coated with 1-30 nm thermal SiO₂, we find that dense thermal oxides of 5 nm or more severely impede lithiation, whereas 1 nm SiO₂ allows lithiation to proceed unimpeded. Intermediate thicknesses of ~3 nm alter the delithiation chemistry while yielding improved CE during galvanostatic cycling. The thickness dependence of peak currents in CV suggests an effect of tunneling through the SiO₂ on reaction kinetics.

The Nature of the Li – SiO2 layer on the Silicon Electrolyte Interface (SEISta)
Silicon Electrolyte Interface Stabilization (SEISta)

Jaclyn Coyle (UC Boulder), Kevin Zavadil (SNL), Kyle Fenton, Josey McBrayer, Chris Apblett (SNL)

Background

This quarter, we have focused on characterizing the electrochemical response, both through cyclic voltammetry and through constant current charge/discharge characterization of the silicon samples coated with silicates containing varying amounts of Li in the SiOx layer. These studies were performed using a standard Gen-2 electrolyte without FEC. We also performed electrochemical impedance spectroscopy on samples exposed to the Gen-2 electrolyte continually, and collected EIS spectra as a function of time and temperature.

Results

LixSiyO CV Studies

Standard samples of thin film Si (50nm Si/500nm Cu/650um C-Si degenerate/100nm Ti/500nm Au) were prepared and diced using the methods previously described. These samples were then used as substrates for the sputter deposition of 40nm thick lithium silicates of varying compositions (SiO_2, $Li_2Si_2O_5$, Li_2SiO_3, and Li_3SiO_x) expected from the tie line on the Li-Si-O ternary for lithiation of SiO_2. These correspond to a 0, 1:1, 2:1, and 3:1 composition of Li:Si. Samples were then assembled into half cells using Li metal as a counterelectrode in a standard coin cell configuration using gen-2 electrolyte (EC:DMC 3:7 1.2M $LiPF_6$) without FEC. Cyclic voltammetry was conducted at 10uV/sec sweeps from open circuit to 0.08V. What was observed was that, in the absence of pre-existing lithium within the oxide, the onset potential for lithiation was observed at 0.23V, in good agreement with other observations for SiO_2 coated Si samples. However, if lithium was present at all in the oxide, the onset potential was significantly higher, near 0.35V, and there were plateaus or peaks that manifested in the lithiation sweep. A first plateau that is present for all lithium containing silicates exists at 0.31V vs. Li/Li+, which does not exist for the pure SiO_2 film. There are additional plateaus/peaks at lower potential, with increasing lithium content in the oxide resulting in an increasing onset potential for the second plateau. It may be that the first plateau is based upon the formation of $Li_{12}Si_7$ with Li inserting into the Si substrate directly from the glass, and the lower potential plateaus onsetting at the formation of $Li_{14}Si_6$ and $Li_{13}Si_4$, respectively, as the amount of available lithium for insertion from the oxide increases. These first cycle CV curves are shown in Figure 1.

Further cycling of the samples in CV result in a steady evolution of both the early onset potential plateau and the lower potential insertions. At the second cycle (see figure 2), SiO_2 now shows some of the peaks observed from the silicates at both the $Li_{12}Si_7$ and $Li_{14}Si_6$ state, and by the 14th cycle the SiO_2 is closely matched to those films with the starting silicates, which potentially match to the onset of the $Li_{14}Si_6$ phase. This suggests that, upon cycling, any native starting oxide is lithiated to behave electrochemically similarly to those oxides that start with lithium in them, suggesting that evolution of the silicon oxide film towards a silicate like structure may be happening. However, evidence of the silicates through direct beam observation are unable to identify these silicates directly, suggesting that it may just be the existence of lithium within the film that gives rise to these effects, rather than for formation of the stoichiometric silicates in the SiO_2 network.

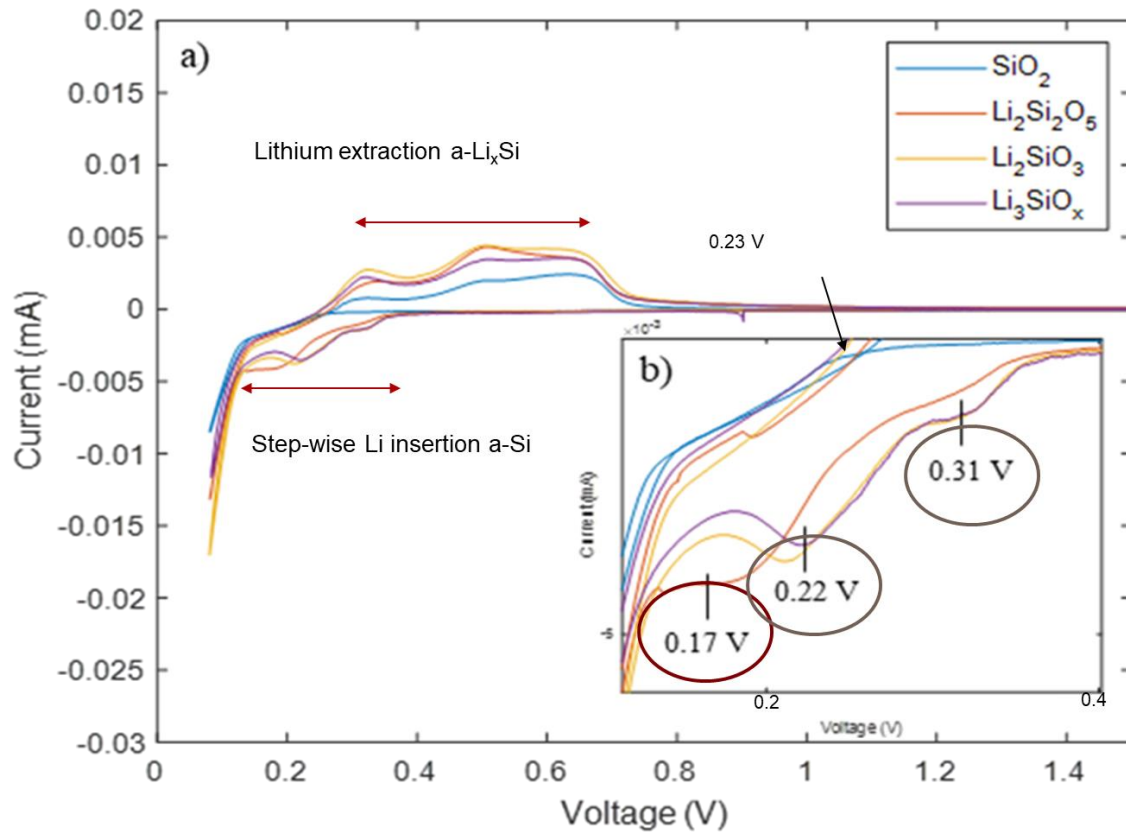First cycle, 0.01 mV/s (~C/50) 1.5V to .08V

Figure 2: CV of 50nm thick SixLiyO films under slow CV. Conditions: 25C, 10uV/sec, 50nmSi/ 500nmCu/ 300umSi/ 20nmTi/ 200nmAu WE, Li CE, Li RE.
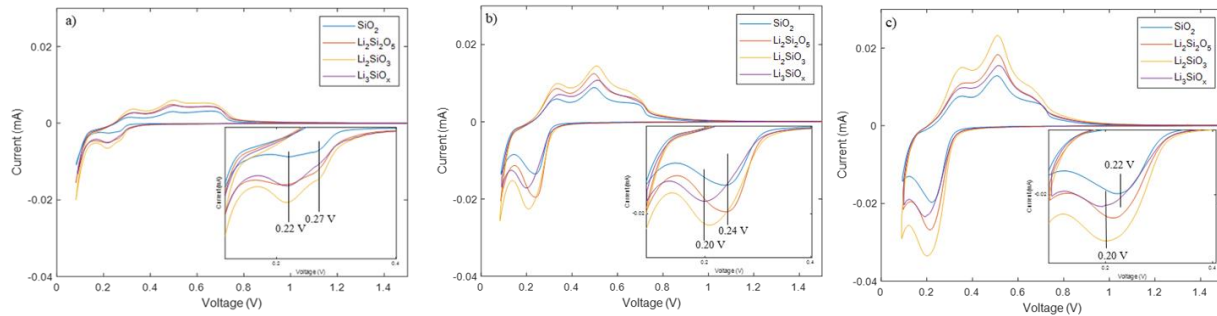

Figure 3: CVs of a) 2nd cycle, b)7th cycle, and c) 14th cycle of SixLiyO samples under slow scan CV (same conditions as above).

Impedance Testing

Electrochemical impedance was completed with each silicate composition exposed to electrolyte at various temperatures and the impedance monitored over time as the films evolved. The resulting impedance curves are very different, with elevated temperatures showing a much changed response over time. SiO2 films exposed to the electrolyte show little change over time at room temperature, with several days of exposure showing minimal change (Figure 3). However, at 60C and 80C (Figure 4), there is significant evolution of the film conditions over time, and at 80C, the equivalent circuit of the resulting response is quite different than in the simple capacitive case, indicating that lithium transport may be affected at the elevated temperatures. In the

19

case of highly lithiated films (such as the Li4SiO4 films), much different impedance response is observed. At

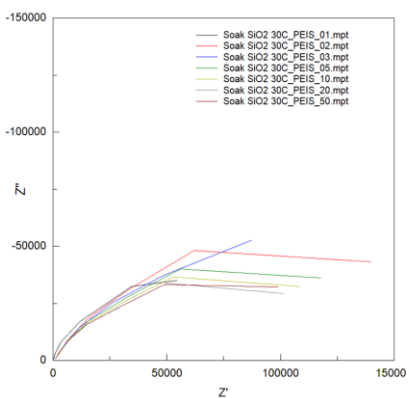

Figure 5: Nyquist plots of SIO2 film exposed to Gen-2 electrolyte at 30C for various times. FIlm evolution is very slow, with little change after several days.
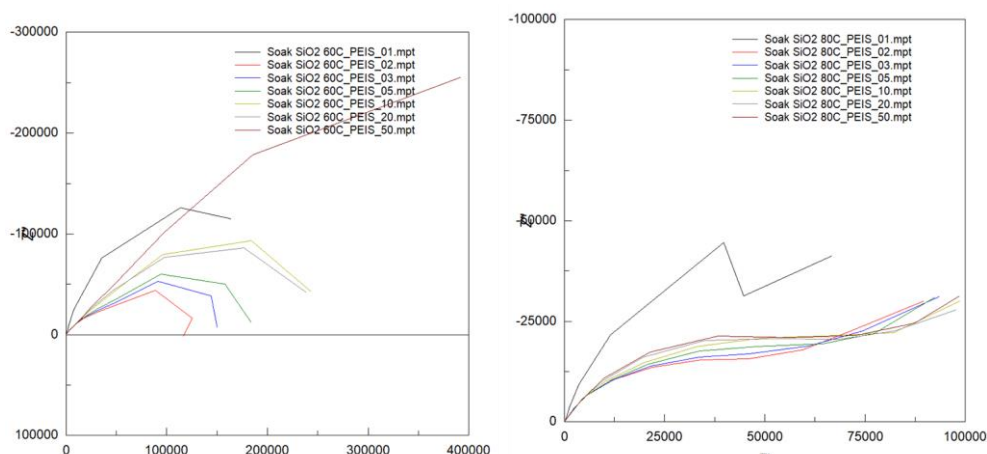

Figure 4: Nyquist plots of SiO2 film exposed to Gen 2 electrolyte at 60C (left) and 80C (right) over time. Both the electrical model and the film evolution are dramatically changed from the room temperature case.

room temperature, after a few hours, the impedance response starts to show signs of a low frequency "loop" in the data, indicative of instability within the electronic response on the timescale of the experiment. At 80C (Figure 5), kinetics of the response are fast enough to remove this low frequency loop, but the evolution of the film is largely complete by the time the first round of EIS is complete, and the film shows little further evolution over time at the elevated temperature. Since the electrical response model is changing depending on chemistry of the film and temperature, it is difficult to coordinate a single set of parameters to extract kinetic properties from the films using EIS solely, so additional techniques will need to be employed going forward to fully develop a kinetic model.

Microcalorimetry
Samples of native oxide, 50nm oxide, and 300nm SiO2 oxide have been prepared by NREL and set up for microcalorimetry in the standard Gen-2 electrolyte. In addition, samples have been prepared of each of the silicates coatings at 50nm (Li2Si2O5, Li2SiO3, and Li3SiOx), and these also have been made ready for microcalorimetry. Tool calibrations have been completed, and the final documentation necessary to begin work have been completed. Once these samples have been measured, they will be compared with the Cu foil samples prepared by ORNL with 50nm Si on Cu foil, with only native oxide on the surface. This will remove

the complications of the degenerate Si located in the silicate samples that could confound the heat flow data. We expect to be able to complete these tests shortly after the new year begins.

Interfacial Stress Measurement
In accordance with **milestone 1**, samples are being prepared for 1, 10, and 50 cycles of bare 50nm silicon directly on the 500nm Cu/300um degenerate Si samples. These will be compared to new samples being prepared of 50nm Si evaporated onto 1mm thick HOPG mirror polished. Since some of the work will involve spectroscopic analysis and in-situ FTIR, the degenerate Si and Cu will not work for these samples, and so a new, IR transparent substrate will need to be characterized. Once done, the measurement of interfacial stress will be started by evaluating several techniques being considered.

Conclusions

Similar to what has been previously observed during chemical only exposure to the electrolyte, the slow scan CV measurements of the silicates have revealed substantive differences between a prelithiated oxide surface and a native SiO2 surface. It is possible that a "pre-lithiation" at the expected potentials for the formation of Li12Si7 and Li14Si6 occurs with Li being supplied from the silicates directly into the Si substrate. After subsequent cycling, the existence of these higher voltage lithiation peaks begin to appear even in the SiO2 coated substrates, and the evolution upon cycling seems to indicate that a final structure of the overcoating
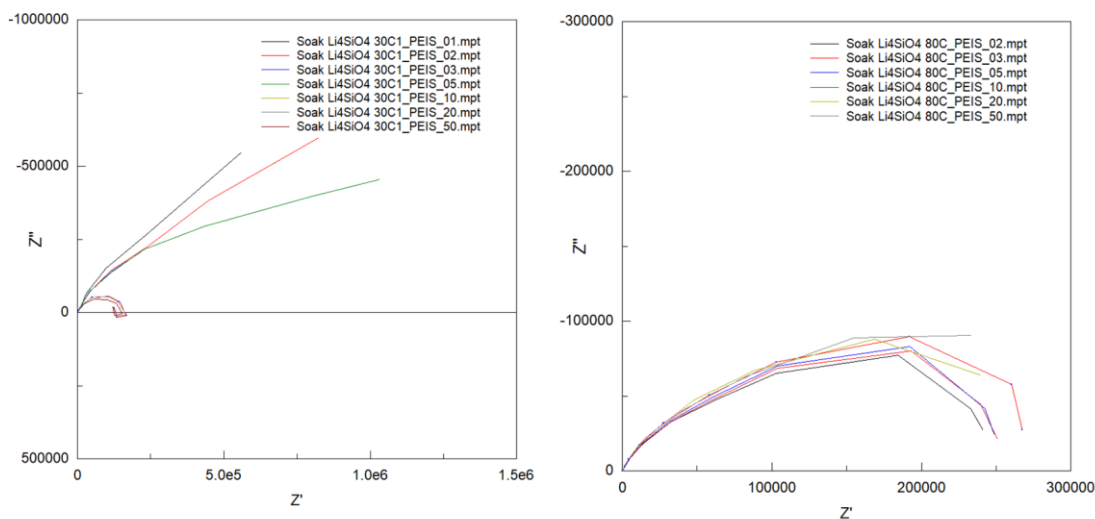

Figure 6: Nyquist plots of Li$_4$SiO$_4$ films exposed to Gen-2 electrolyte over time at room temperature (left) and 80C (right). The lithiated films show instability at low temperature resulting in a low frequency "loop" structure after a few hours. This structure is absent at 80C, which suggests that the film evolution of the highly lithiated silicates completes quickly, and does not further evolve over time.

material evolves within a few cycles to accommodate the formation of Li14Si6. EIS also shows dramatic differences between unlithiated and lithiated model SEIs, with very little evolution occurring at room temperature, but different mechanisms beginning to occur at elevated temperatures. With high lithiation in the SEI, the evolution of the film proceeds more quickly.

Chemical and Electrochemical Reactivity of Plasma-Synthesized Silicon Nanoparticles

Mike Carroll, Greg Pach, Bertrand Tremolet de Villers, Nate Neale (NREL)

Background

One of NREL's tasks explores plasma-synthesized silicon nanoparticles (Si NPs) as model systems for Li_xSi anodes. Such plasma-prepared Si NPs are valuable since they feature hydrogen-passivated surfaces and a high surface area resulting from their <10 nm diameter that makes them well suited for chemical reactivity studies using Fourier transform infrared (FTIR) spectroscopy and quantitative off-gassing analysis. These reactivity studies are relevant for understanding (1) early-stage SEI layer growth as well as (2) individual SEI component chemical stability. In early FY19, we continued our prior years' efforts to (1) develop an operando ATR-FTIR capability for studying early-stage SEI grown and dissolution; (2) increase the size and scale of our Si NP plasma production process; and (3) started a new effort to incorporate plasma-grown Si NPs into batteries.

In Q1FY19 we conducted an analysis of the first electrochemical cycling of SEISta "pristine" Si wafer samples under electrochemical polarization in a half-cell configuration along with operando ATR-FTIR spectroscopy. We added an inductively-coupled plasma capability to our growth system that in the first run gave larger 24.5±7.0 nm diameter Si NPs relative to the 19.9±3.7 nm diameter NPs we demonstrated previously from capacitively-coupled plasma growth. In addition, we have continued to prepare several ~200 mg batches of ~7 nm diameter Si NPs. Finally, additional new work for Q1FY19 is that these plasma-grown Si NPs are being fabricated into batteries to study the effects of oxidation and surface chemistry on early-stage SEI growth correlated with coin cell battery performance.

Results

Operando ATR-FTIR Spectroscopy. In Q1FY19, we have continued our development of the operando attenuated total reflectance-Fourier transform infrared (ATR-FTIR) spectroelectrochemical characterization instrument. Prior work in this area by Phil Ross and coworkers[1,2] showed that the components of the SEI vary significantly as a function of applied voltage. An electrolyte comprised of 1.0 M $LiPF_6$ in EC:DEC (1:2, v/v) was used in conjunction with native oxide (SiO_x)-covered Si wafer. At 1.3 V, electrolyte reduction (DEC) to diethyl 2,5-dioxahexane dicarboxylate (DEDOHC) was found, whereas at 5 mV, selective electrolyte reduction (EC) to lithium ethylene dicarbonate (LiEDC) occurs.[3] Cycling data showed a SEI composed primarily of DEDOHC. Our goal is to extend this study SEI dissolution and growth using other model samples (H-terminated Si, native SiO_x-terminated, and molecularly-functionalized Si wafers) and eventually extend this to three-dimensional Si NP-based electrodes assembled on the Si wafer substrate.

Our new setup provides significant advantages over that of Ross and coworkers, who used several milliliters of electrolyte in their operando experiments. Since it is well-known that SEI dissolution and growth is strongly dependent on the electrolyte volume, we designed our ATR-FTIR cell to be effectively that of a coin cell where a Celgard separator is placed directly on top of the double-polished Si wafer. The Si wafer in this configuration doubles as the ATR crystal *and* the working electrode. A Li metal foil counter electrode is placed on top of the Celgard separator, followed by a stainless-steel plate and rod. The stainless-steel plate and rod applies pressure to the electrode assembly to more closely mimic that of a coin cell battery as well as minimize the air gap between the ZnSe ATR prism and the double-polished Si wafer.

In Q1FY19, we discovered that our cycling data had a significant voltage offset due to a poor contact to the Si wafer substrate. We estimate that a 1–2 kΩ resistor owing to this bad contact can account for the ~300 mV offset observed in the voltage profiles for our current density and galvanostatic cycling data (Figure 1). Fixing this issue so that we can perform cycling studies relevant to the SEISta Milestones of exploring SEI dissolution and growth at specific voltages (1.5, 1.0, 0.7, 0.4, 0.15 and 0.05 V vs Li/Li^+) and current densities will be a priority in FY19.
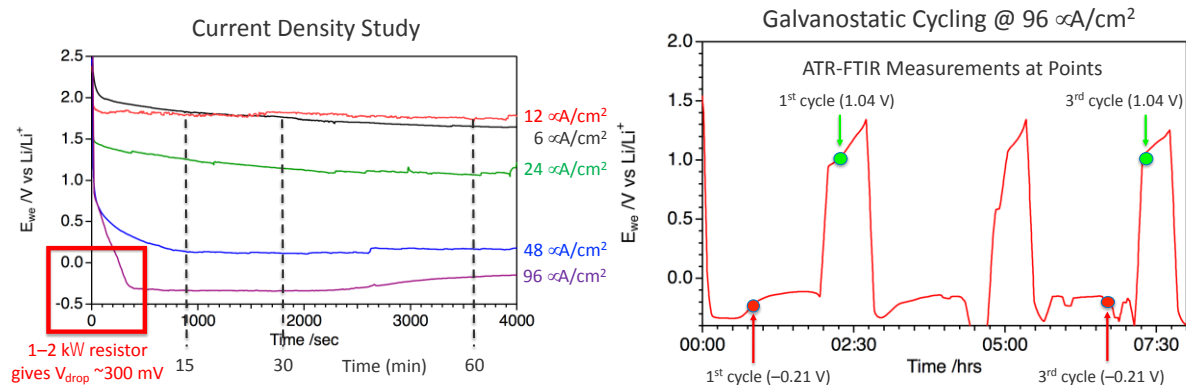
Figure 1. Left: Current density study for 5–10 $\Omega\cdot$cm resistivity Si wafers in the ATR-FTIR spectroelectrochemical cell. A voltage drop of ~300 mV is caused by a poor contact to the Si wafer. Right: Cycling behavior of the same cell indicating points where ATR-FTIR spectra were collected (see Fig. 2 for ATR-FTIR data).

Still, we have analyzed our preliminary experiments with this operando ATR-FTIR cell for native oxide SiO_x|c-Si wafer in Gen2 electrolyte with 10% FEC in a half-cell configuration and find promising results. Note that Gen2 with 10% FEC was the only electrolyte available for this preliminary experiment, and late in Q1FY19 we finally received new Gen2 electrolyte that will be used exclusively going forward to align with the SEISta project. Figure 2 (top) shows ATR-FTIR spectra on the SiO_x|Si working electrode was taken at open circuit (black) and following cycling down to –0.21 V and up to 1.04 V (vs. Li^+/Li^0 reference electrode; again ca. 300 mV voltage offset is due to a resistive contact) on the 1st and 3rd cycles (red and green spectra, respectively) at a current density of 96 µA cm^{-2}. Yellow highlighted regions indicate loss of signal during cycling and green highlighted regions show areas that express growth and dissolution of SEI during cycling. The difference spectra (Figure 2, bottom) are clear that EMC, unique to the Gen2 electrolyte and significantly different from the earlier studies by Ross and workers, provides the greatest change near the electrode surface. The intensity of the FTIR modes of EMC coordinated to Li^+ ions decrease substantially upon cycling, showing local depletion of this complex. Concomitantly, an increase in uncoordinated EMC is observed. This suggests that early-state SEI growth stems from extraction of Li^+ ions from the $Li(EMC)_x$ complex, where $x = 4,5$, or 6 as per Kristin Persson's calculations under the SEISta project. In contrast, relatively little change in the concentration of near-surface $Li(EC)_x$ complex is found, suggesting that future efforts should focus on the linear carbonates as sources of Li^+ ions for SEI growth.
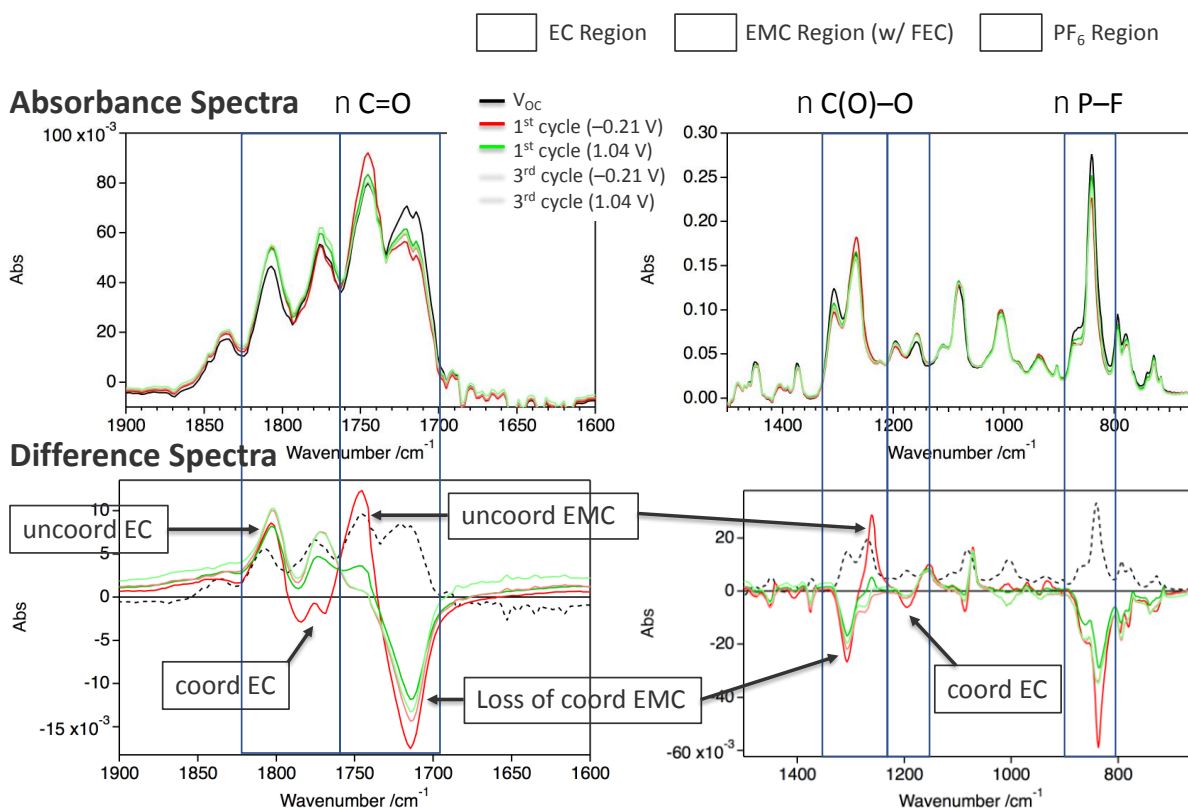
Figure 2. Left: Operando ATR-FTIR spectroelectrochemical cell data for native oxide SiO_x|c-Si wafer in Gen2 electrolyte with 10% FEC in a half-cell configuration. ATR-FTIR spectra on the SiO_x|Si working electrode was taken at open circuit (black) and following cycling down to –0.21 V and up to 1.04 V vs. Li^+/Li^0 on the 1st and 3rd cycles at a current density of 96 μA cm^{-2} (red and green, respectively). Yellow highlighted regions indicate loss of signal during cycling and green highlighted regions show areas that express growth and dissolution of SEI during cycling. The top two spectra are absorbance and the bottom two spectra are difference spectra relative to the OCV data (dashed black data).

Silicon Nanoparticle Production via Nonthermal Plasma Synthesis. In FY18, we found that our capacitively-coupled plasma (CCP) system could be used to generate 19.9±3.7 nm NPs. Subsequent efforts to optimize growth conditions using this CCP system did not increase Si NP size far beyond an average of 20 nm in FY18. Midway through Q1FY19, a white paper to expand and accelerate the plasma growth process was accepted by DOE. Though funds still haven't arrived at Q1FY19 end, we have begun executing this new enhanced effort using FY18 carryover funds with the assumption that additional required support will be allocated in the near future.

In Q1FY19, we developed an inductively-coupled plasma (ICP) system that literature reports show can be used to generate far larger ~100 nm diameter Si NPs. [3] We are pleased to report that our first attempt at using this new IPC system generated 24.5±7.0 nm diameter Si NPs (Figure 3). Notably, with a substantial fraction of the NPs were larger than 30 nm in diameter, which suggests that further optimization should increase particle size on the order of 50–100 nm.

The other parts of this expanded and accelerated plasma growth effort also were begun in Q1FY19, namely posting a job requisition and recruiting for a new hire growth technician. This new plasma reactor operator will be hired in Q2FY19 and fully explore the reactor parameter space of gas flow rate, gas composition, pressure, delivered plasma power, etc. This new hire additionally will be assigned work to optimize growth conditions for producing quantities of at least 5 g of Si NPs per week and ideally achieve a greater diameter than the ~25 nm diameters achieved thus far. This person additionally will allow us to provide a more regular supply of samples to external collaborators (e.g., John Zhang, vide infra).
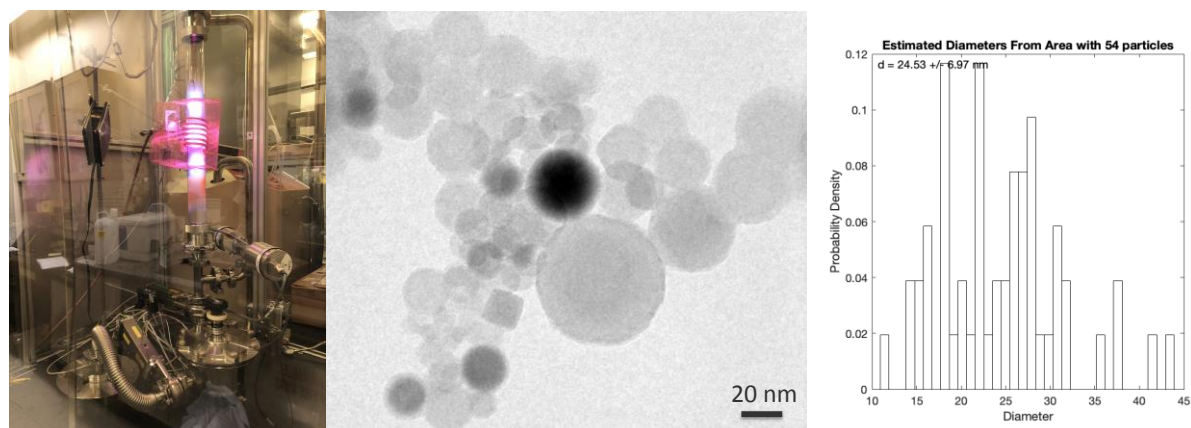
Figure 3. Left: Inductively-coupled plasma system during growth of Si Nps. Middle: TEM image of ICP-synthesized Si NPs from the first growth run. Right: TEM histogram analysis showing 24.5±7.0 nm diameter Si NPs with a large fraction of particles >30 nm.

Oxygen-, Water- and Graphite-Free Silicon Nanoparticle Batteries. I am aware that the research community has a strong desire for larger-sized NPs approaching 100–200 nm in diameter. Given what we have learned in SEISta thus far and the fact that I am unconvinced any R&D team has actually studied Si (every commercial supplier provides heavily oxidized Si NPs that can be up to 80% SiO_x (!) as per Baris Key's solid-state NMR and my own FTIR analyses), I think we cannot *a priori* make any statement that larger Si NPs will perform better than smaller Si NPs. In fact, charging rate may be enhanced significantly using smaller Si NPs owing to the more rapid Li-ion diffusion through only several nm of material.

Thus, a major effort in FY19 will be spent correlating SEI early stage growth and dissolution with performance of Si NPs in batteries. Our goal is to study surface-functionalized Si NPs fabricated into batteries *air-free*, and in doing so understand how the Si NP surface bonding structure impacts the evolution of the SEI and stability of the electrodes as well as deconvoluting the impacts of oxide versus surface chemistry. In Q1FY19, we assembled all of the necessary capabilities for preparing such air-free Si NP electrodes, including a slurry mixer, blade caster, etc. as shown in Figure 4. In addition, we prepared all of the chemistries necessary for this study including in-house purified N-methyl-2-pyrrolidone (NMP), in-house purified polyacrylic acid (PAA) binder, and a set of polyether-functionalized Si NPs given our previous work on chemical reactivity showing that silyl ether moieties (Si–O–C) are stable toward Gen2 electrolyte. We successfully prepared our first set of air-free Si NP batteries using these methods and will be reporting our early cycling data in Q2FY19. We are working closely with John Zhang at Argonne National Lab, who is performing similar studies using samples of NREL's plasma-synthesized Si NPs and the standard Silicon Deep Dive 15 wt% Si, graphite-based electrodes fabricated in air.
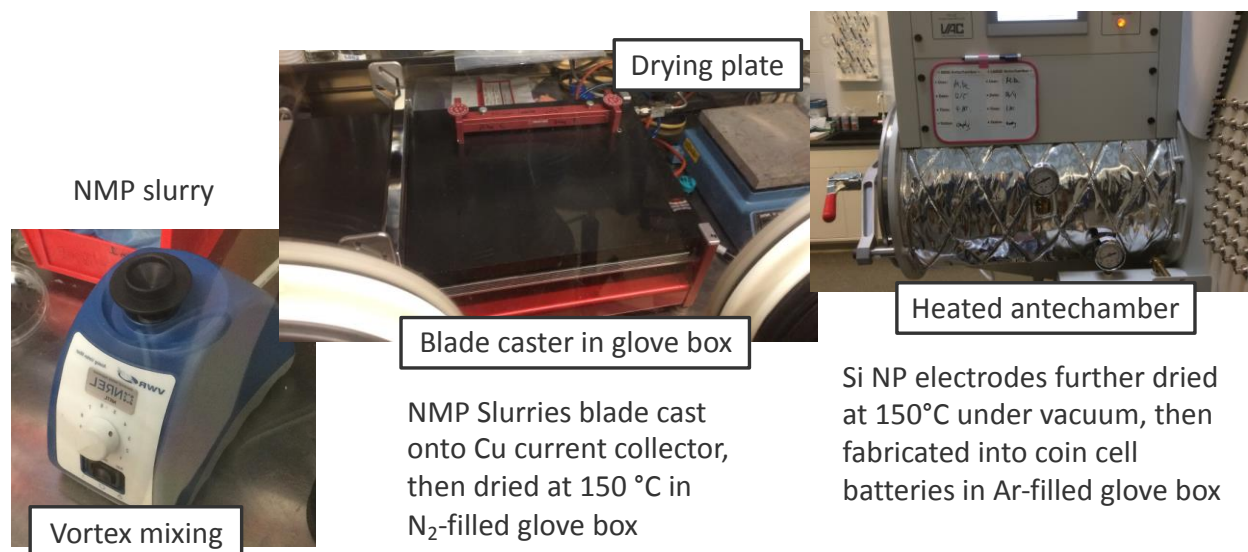
Figure 4. Capabilities for fabricating graphite-free Si NP-based electrodes under oxygen- and water-free conditions.

Conclusions

Summary of Q1FY19 is:

- ATR-FTIR spectroelectrochemical cell is operational, and studies of early-stage SEI dissolution and growth will be conducted upon fixing the contact issue to the Si wafer substrate. The operando ATR-FTIR spectrochemical instrument will be leveraged to understand SEI growth and dissolution on model SEISta planar samples for pristine, native oxide, and surface-functionalized samples in Gen2 electrolyte both with and without 100 ppm water in direct support of FY19 SEISta Milestones.
- Inductively-coupled plasma synthesis provides larger Si NPs than does capacitively-coupled synthesis.
- Hiring a full-time growth technician to accelerate development of the plasma growth process is underway.
- Capabilities to fabricate oxygen-, water- and graphite-free Si NP electrodes have been assembled. Planned studies for FY19 include separating the effects of oxidation and surface chemistry on SEI formation and stability in both batteries as well as operando ATR-FTIR experiments.

References

1. Shi, F.; Ross, P. N.; Zhao, H.; Liu, G.; Somorjai, G. A.; Komvopoulos, K. *J. Am. Chem. Soc.* **2015**, *137*, 3181.
2. Shi, F.; Ross, P. N.; Somorjai, G. A.; Komvopoulos, K. *J. Phys. Chem. C* **2017**, *121*, 14476.
3. Bapat, A.; Perrey, C. R.; Campbell, S. A.; Carter, C. B.; Kortshagen, U. *J. Appl. Phys.* **2003**, 94, 1969.

How the Silicon Surface Affects the Silicon Electrolyte Interface Stabilization (NREL)-

Yanli Yin, Elisabetta Arca, Caleb Stetson, Andrew Norman, Chun-Sheng Jiang, Mowafak Al-Jassim (PI), Glenn Teeter (PI), Chunmei Ban (PI), NREL, Golden, CO

Background

Experimental work for this quarter is focused on preparation and characterization of SEI on two model Si surfaces: native SiO_x on Si wafer and 5-nm thermally grown SiO_2 on Si wafer. Compared with the native SiO_x, thermally grown SiO_2 is more insulating: the electrochemical behavior of lithiation and delithiation processes is expected to show significant differences between native SiO_x and 5-nm SiO_2. The electrochemical behavior

of the early-stage SEI, decoupled from the lithiation behavior of Si, is measured to further investigate this difference. The SEIs formed on these two distinct surfaces were also analyzed (via XPS, AFM, SSRM) in their pristine state and after 1, 10 and 50 cycles of lithiation and delitiation. Analysis of these two model systems isolates the impact of the insulating layer on SEI formation on the Si wafer electrode system.

Results

Experimental Method. Silicon (Si) model samples with native SiO_x layer and 5-nm SiO_2 established in FY17 have been used in this study. All of the silicon electrodes (½ inch x ½ inch) were cleaned with our established multi-step cleaning protocol to remove the surface grease, particles and organic residue. After cleaning, the electrodes were dried in vacuum oven at 100 °C prior to the cell fabrication. The electrolytes selected for this research are 1.2 mol/L $LiPF_6$ (abbreviation "G2" used in the plots) dissolved in the solution comprised of ethylene carbonate (EC): ethyl methyl carbonate (EMC) with the weight ratio of 3:7, respectively. All of the Si electrodes were used as work electrodes in the customized electrochemical cells, where the lithium metal was used as a counter electrode. 7 µl of the electrolyte was used in every cell; and the Celgard 2325 was used as a separator for the cell assembly. After cycling, samples were dimounted, washed in dimethyl carbonate (DMC) for two minutes, dried in vacuum for one hour, then transferred to a glovebox atomic force microscope (AFM) system or to an X-ray Photoelectron Spectroscopy (XPS) system through a system of gloveboxes and vacuum chambers, to avoid exposure to atmosphere.
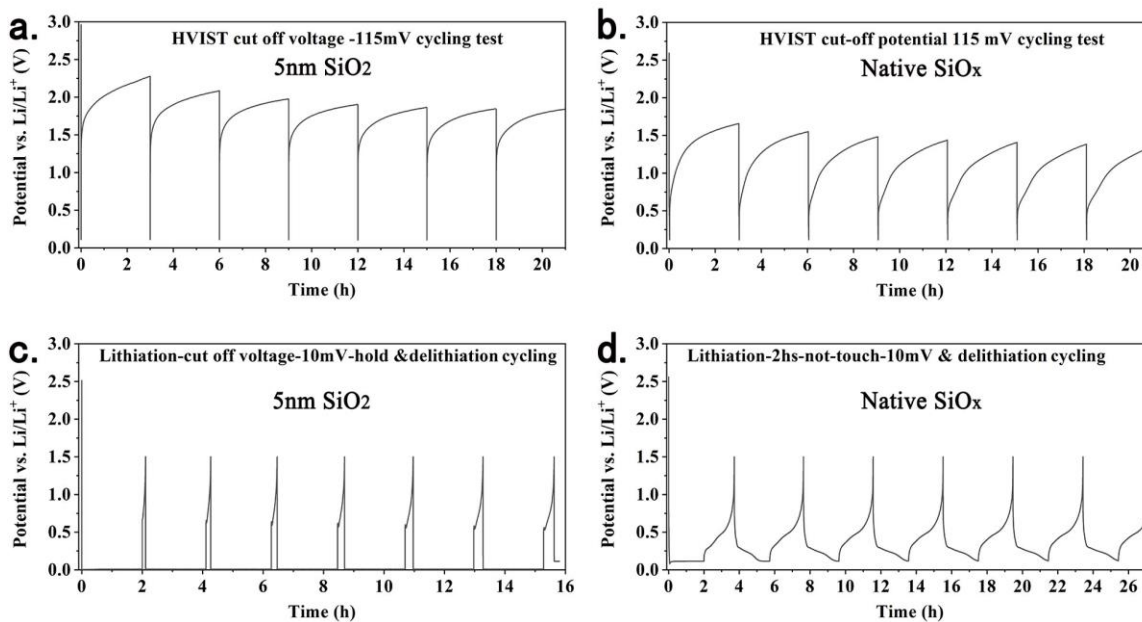
Results and Discussion.

Fig. 1. The voltage profile under the HVIST condition with the cut off voltage at 0.115 V including only early-stage solid-electrolyte interphase (es-SEI) formation on (a) 5-nm SiO_2 and (b) native SiO_x, respectively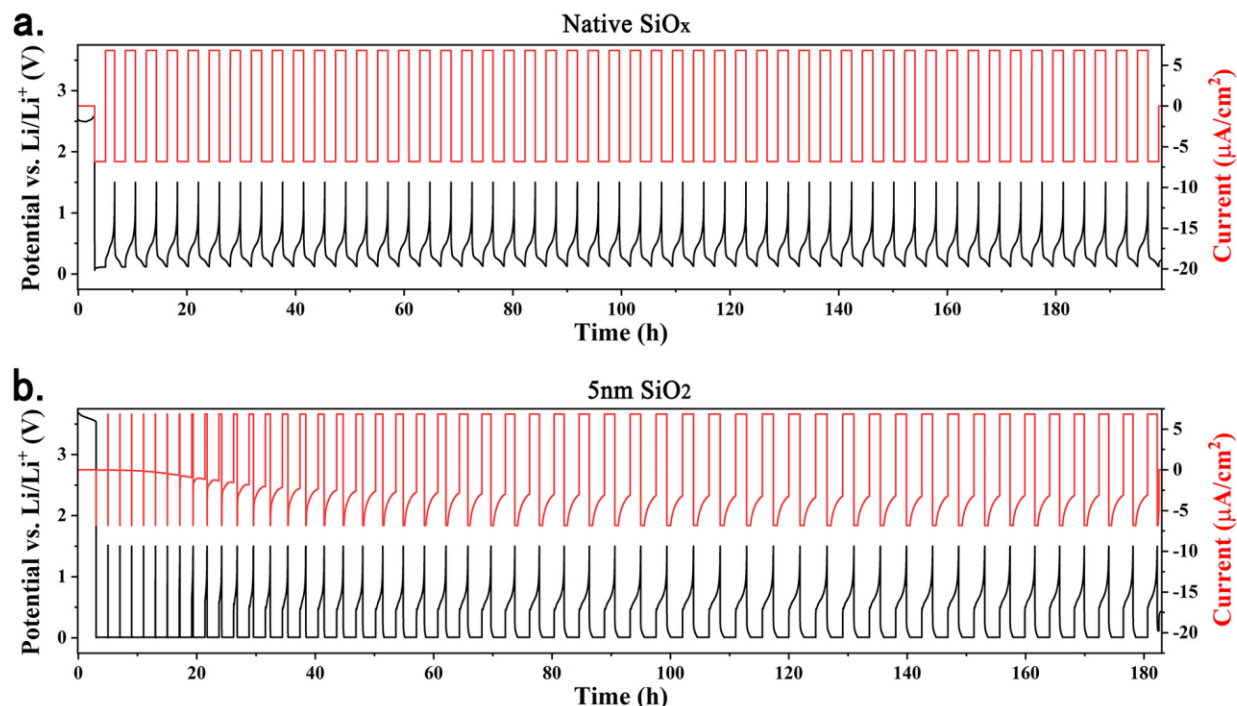. The voltage profile under the regular condition with cut off voltage at 0.010 V and 2 hours' time limitation including both SEI formation and Si lithiation on (c) 5-nm SiO_2 and (d) native SiO_x, respectively.

We ran a high voltage interphase stabilizing testing (HVIST) procedure reported in FY18 Q3 on the 5-nm SiO_2 and native SiO_x, respectively: apply a galvanostatic reduction current of 6.82 µA cm^{-2} with the cut off voltage at 0.115 V, then rest for 3 hours, repeat for seven cycles. Figure 1a and 1b show the voltage profiles as a function of time under this HVIST procedure on 5-nm SiO_2 and native SiO_x, respectively. SEI phases form at the electrode/electrolyte interface via electrolyte reduction driven by electrons supplied by the electrodes. Here, the more electrically insulating surface of the 5-nm SiO_2 layer results in less electrolyte reduction in comparison with the native SiO_x case. Therefore, the profile of 5-nm SiO_2 shows a higher final open circuit voltage (OCV) during the rest process than does the native SiO_x case. We ran a regular procedure of lithiation and delithiation on the 5-nm SiO_2 and native SiO_x, respectively: application of a 6.82 µA cm^{-2} galvanostatic

reduction current for time up to 2 hours, with the cut off voltage at 0.010V, followed by an oxidation current (6.82 μA cm^{-2}) to 1.5 V, repeated for seven cycles. Figure 1c shows the voltage profile as a function of time under this regular condition on the 5-nm SiO_2, which has the quick drop to touch 0.010 V in every cycle followed by a holding at 0.010 V. The profile shows a continuous increase of time in delithiation process with cycle number, which may be attributed to the increase of the lithiation with cycle number. This indicates that the insulating surface of 5-nm SiO_2 is continuously changing to be conductive. We define this behavior of surface as being "activated".

Fig. 2. The voltage profile in 50 cycles under the regular condition with cut off voltage at 0.010 V and 2 hours' time limitation including both SEI formation and Si lithiation on (a) native SiO_x and (b) 5-nm SiO_2, respectively.

We continued running the regular procedure of lithiation and delithiation for as long as 50 cycles on the native SiO_x sample and 5-nm SiO_2 sample, respectively. Figure 2a shows the voltage profile as the function of time for native SiO_x sample. During the 50 cycles, the native SiO_x sample shows reversible of lithiation/delithiation behavior. Figure 2b shows the voltage profile as a function of time for 5-nm SiO_2 sample. During the first few cycles, the 5-nm SiO_2 sample shows the passivated performance without lithiation and delithiation behavior. During the first 20 cycles, the lithiation current of the 5-nm SiO_2 sample gradually increases during the cut off voltage holding process. The delithiation time gradually increases as well, which indicates an increasing degree of lithiation and delithiation. After the first 20 cycles, the lithiation and delithiation behavior of 5-nm SiO_2 sample is repeatable which indicates that the previously insulating surface has been "activated".
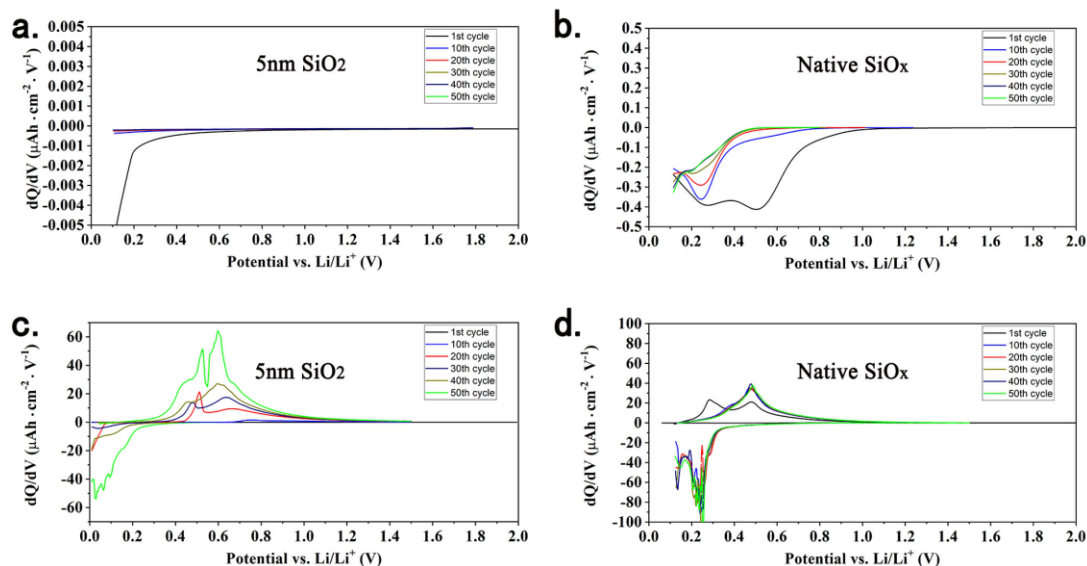
Fig. 3. The differential capacity profile under the HVIST condition with 0.115 V cut-off voltage, including only es-SEI formation on (a) 5-nm SiO$_2$ and (b) native SiO$_x$, respectively. The differential capacity profile in 50 cycles under the regular condition with 0.010 V cut-off voltage and 2 h time limitation including both SEI formation and Si lithiation on (c) 5-nm SiO$_2$ and (d) native SiO$_x$, respectively.

Figure 3a shows the differential capacity profile as a function of potential for the 5-nm SiO$_2$ sample under HVIST condition. Over the course of 50 cycles, the 5-nm SiO$_2$ sample shows no reactive peak after the 1st cycle, which indicates the insulating nature of the sample surface. Figure 3b shows the differential capacity profile as a function of potential for native SiO$_x$ sample under HVIST condition. In the first cycle, an electrolyte reduction peak is observed at around 550 mV, and a second reduction peak at 250 mV might be associated with native SiO$_x$. During the subsequent cycling, the peak at 550 mV disappears after about 10 cycles, while the peak at 250 mV reduces slowly and disappears after the 50 cycle.

Figure 3c shows the differential capacity profile as a function of potential for 5-nm SiO$_2$ sample under regular lithiation and delithiation condition. During the 50 cycles, the intensity of both the reductive and oxidative peaks continuously increases, showing that the insulating surface is repeatedly "activated". Figure 3d shows the differential capacity profile as a function of potential for native SiO$_x$ sample under regular lithiation and delithiation condition. After 1st cycle, two pairs of reductive and oxidative peaks appear in each cycle, consistent with the formation of an amorphous silicon layer.[1-2] XPS measurements were performed to determine the species present at the surface.
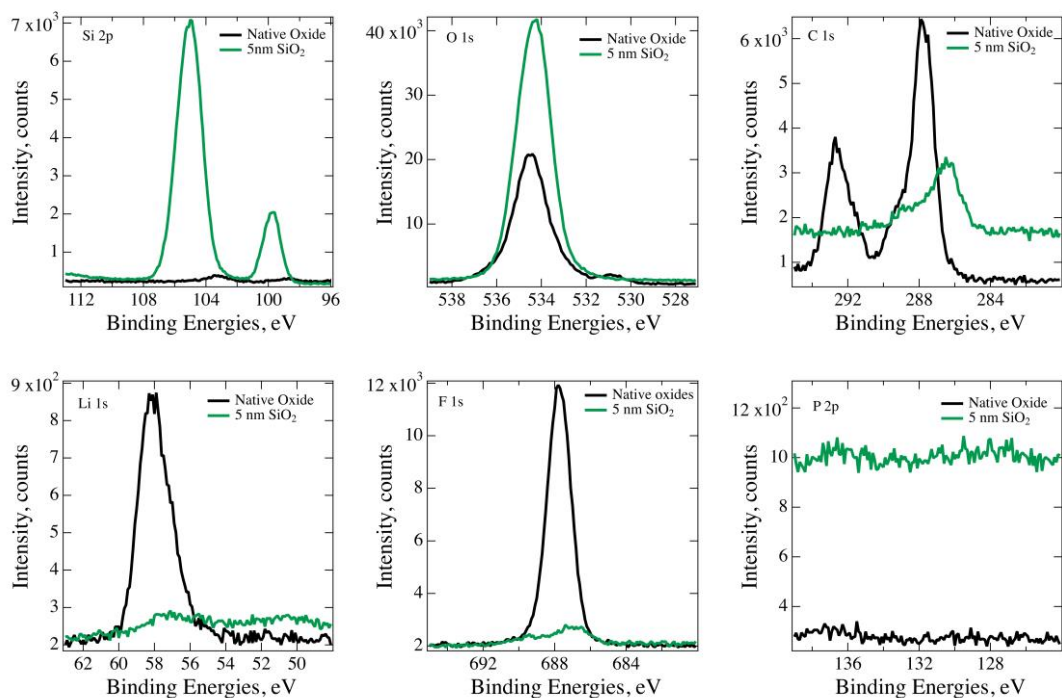
Fig. 4. Comparison of XPS core levels measured for a sample terminated with native oxide and a sample terminated with 5 nm SiO₂ measured after cycling (lithiation/delithiation cycles for 2h, 10 cycles, final potential 115 mV)

Comparison between the 5-nm SiO_2 and native oxide sample reveals substantial differences in the SEI present at the surface, both in terms of its thickness and composition. This is valid for all stages of the HVIST process which were analysed. As an example, we are reporting the case of lithiation/delithiation cycles for 2h, 10 cycles, final potential 115 mV for both native oxide and 5-nm SiO_2 samples as shown in Fig. 4. The native oxide sample shows a much thicker SEI, demonstrated by the higher concentration of element such as C, F and Li, and by the fact that the intensity of the Si peak is strongly attenuated. The fact that the Si peak is barely visible indicates that the thickness of the SEI is only slightly less than the probe depth of the XPS measurements.

To determine the composition of the SEI, peak fitting was carried out on each core level. Fig. 5 shows that the SEI formed on the native oxide sample comprises a large fraction of organic and inorganic carbonates, ester and/or carboxyl groups, LiF, and Li_2O_2 as main components. The 4th additional component in the oxygen is due to the residual SiO_x, although it is unclear at the moment if the latter was converted into a silicate phase.
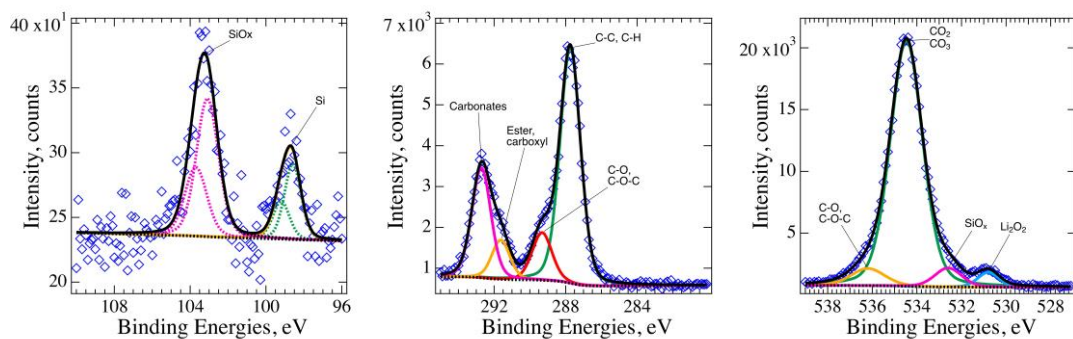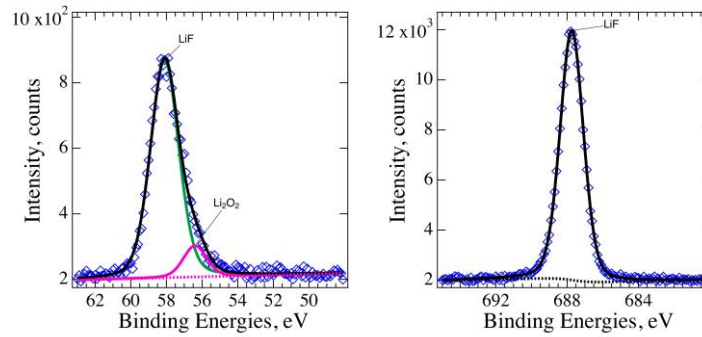
Fig. 5. Chemical states associated with the SEI formed on the native oxide sample determined by peak-fitting analysis.

For comparison, the same analysis was performed on the 5-nm SiO_2 sample, as shown in Fig. 6. When comparing the composition between the two samples, the lack of carbonate species is the most noticeable difference. Only a small amount of ester or carboxyl group is noticed in terms of organic components of the SEI. The inorganic components are due to LiF and Li_2O_2, although their concentration is much reduced in comparison to the previous sample. One component on the fluorine core level remains unassigned. Most of the oxygen present at the surface is due to SiO_2. Looking closer into the O 1s core level peak fitting, it is noticeable that the position of the SiO_2-related component and that of ester/carboxyl groups, are reversed in comparison to the previous sample. This difference might be due differential charging effects, due to higher electronic conductivity of the SiO_x layer in comparison to the SiO_2 layer, or due to a change in the composition of the SiO_x matrix. Closer analysis of the Si core level reveals that the binding energy separation between the SiO_2-related components and the elemental Si component is different in the two samples being 5.26 eV for the 5 nm SiO_2 sample and 4.50 eV for the native SiO_x sample. Further analysis is underway to try to determine the exact root-cause of this difference.
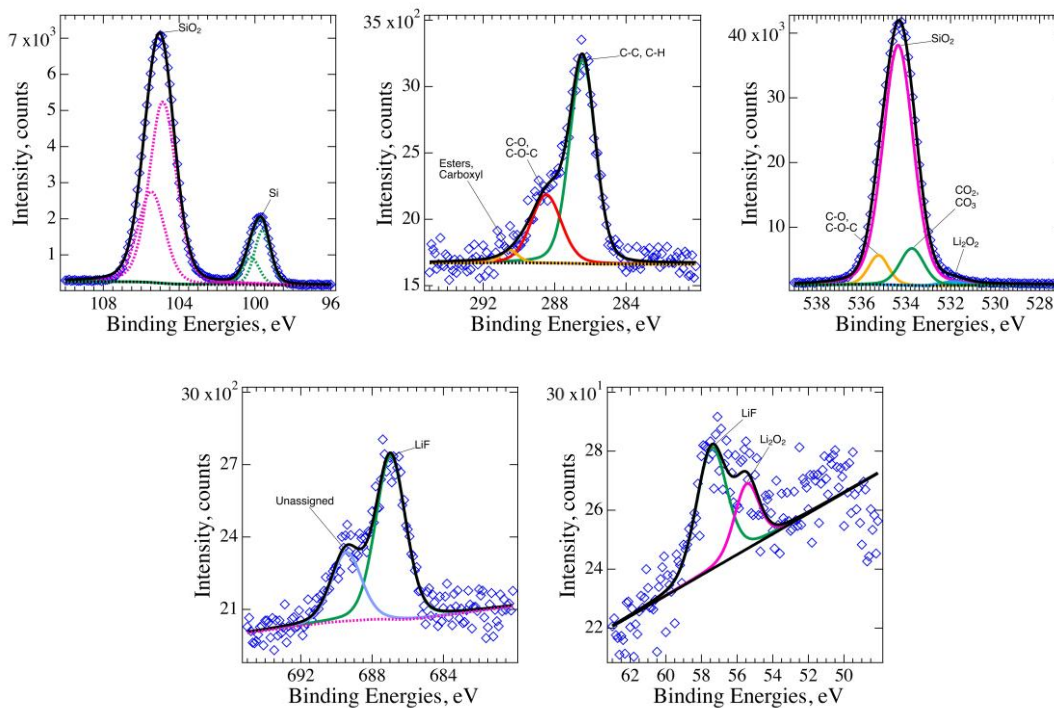

Fig. 6. Composition of the SEI formed on 5 nm SiO_2 sample determined by peak-fitting analysis
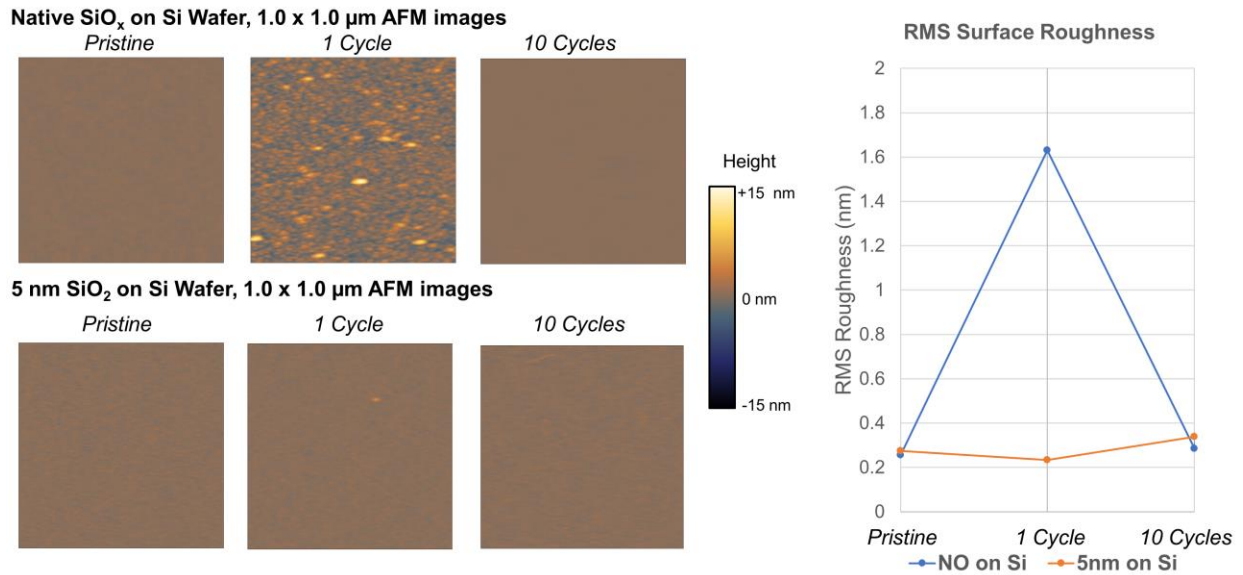
Fig. 7. AFM morphology characterization of SEIs formed on two model Si surfaces.

AFM morphology was measured at increasing scan sizes until surface roughness saturated, allowing for quantification of RMS roughness. 1.0 x 1.0 µm AFM images show qualitative comparison of the surfaces. On the native SiO_x on Si wafer system, roughness was seen to increase significantly through SEI formation in the initial cycle, followed by a significant reduction in roughness by 10 cycles. This change in SEI morphology from 1-10 cycles is likely a result of kinetic behavior at the surface leading to stabilization and evening on the surface, and may also be indicative of changes in SEI solubility. On the thermally grown 5-nm SiO_2 on Si wafer system, this trend was not observed; roughness was roughly equivalent between the pristine surface and the 1 cycle SEI, with a slight increase for the 10 cycle SEI.

SSRM 3D resistivity vs. depth profiling was performed for each of samples depicted above.[3] Results showed distinct differences between the electronic resistivity of the SEIs formed on the two model systems.
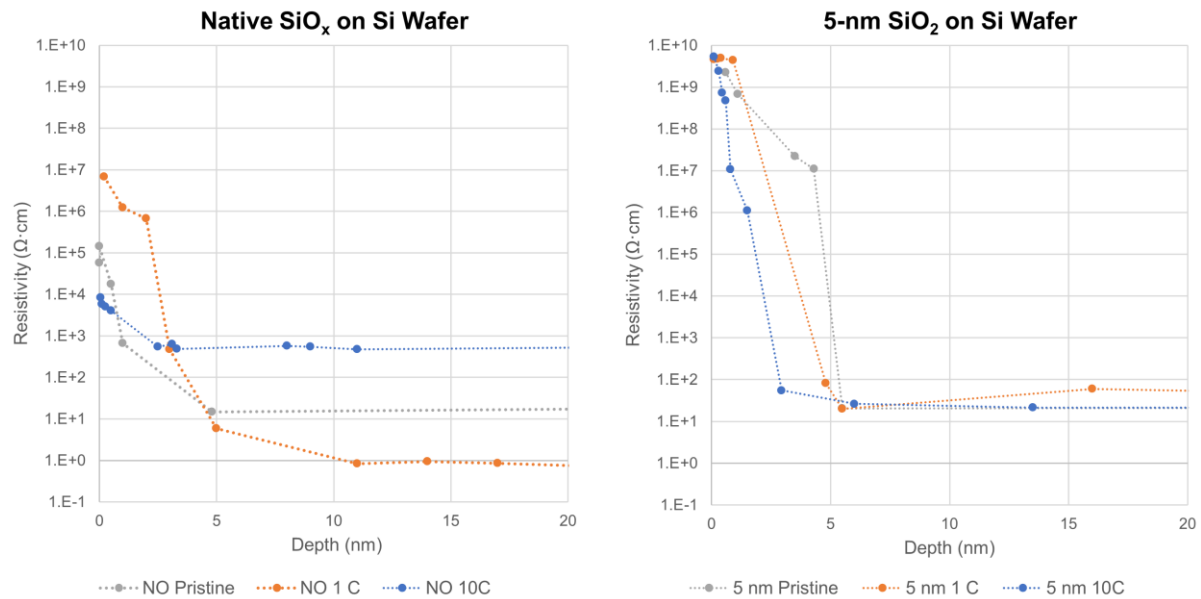

Fig. 8. SSRM resistivity vs. depth profiling of SEIs formed on native SiO_x and thermally grown 5-nm SiO_x.

Resistivity vs. depth profiles showed higher electronic resistivity for the SEIs formed on thermally grown 5-nm SiO_2 when compared to SEIs formed on native SiO_x. This relative difference in electronic resistivity of SEIs is likely due to the greater relative composition of inorganic species (LiF, Li_2O) for SEIs formed on native SiO_x on Si, which has been shown to be responsible for lower measured resistivity in previous SEISta works.

SEI formed on native SiO_x was measured to be thicker than SEI formed on thermally grown 5-nm SiO_2. On both model systems, SEI was shown to be thinner after 10 cycles when compared to SEI formed after one cycle. As with observed differences in surface morphology on cycled native SiO_x, the reduced thickness at a later stage of cycling is likely due to shifting solubility of SEI phases through cycling and SEI stablization.

Comparison of the mechanical properties of the formed SEIs on 5-nm SiO_2 and the pristine thermally grown 5-nm SiO_2 reveals that mechanical hardness is greater for the original pristine oxide when compared to the formed SEIs; moreover, measured SEI thicknesses for the formed SEIs on the same system were thinner and less resistive, indicating that the SiO_2 film is transformed or displaced during the first electrochemical cycle.

Resistivity of the underlying Si was shown to change for the native SiO_x on Si through cycling, while the thermally grown 5-nm SiO_2 showed little to no change to the resistivity of the underlying Si through cycling from 1-10 cycles. The observed differences in the resistivity of native SiO_x before and after cycling show the trend $\rho_{10\text{-}cycles} > \rho_{pristine} > \rho_{1\text{-}cycle}$, indicating that the first cycle inserts Li while preserving the Si-Si bonds leading to an overall increase in electronic conductivity; after 10 cycles, lithiation has disrupted Si-Si bonds such that overall electronic conductivity is lower than the original Si prior to cycling.[4] These relative differences in electronic resistivity data were steadily observed for measurement depths in excess of 100 nm into the Si anode. Based on electrochemical cycling data, particularly current vs. time plots, less lithiation occurs during initial cycles on the 5-nm SiO_2 on Si system (prior to "activation" of the insulating SiO_2 surface), which may explain why the same trend in the electronic resistivity of Si was not observed for this model system from 1-10 cycles.

Conclusions

SEIs formed on native SiO_x and 5-nm thermally grown SiO_2 on Si wafer showed major differences in structure, composition, electronic properties and electrochemical behavior. Electrochemical results show an "activation" of the 5-nm SiO_2 surface through the first 20 cycles, corresponding to an irreversible increase in conductivity of the surface thin film. SEIs formed on native SiO_x on Si were thicker, as determined by XPS and SSRM. XPS results showed that SEI formed on native SiO_x showed greater C, Li, and F content. SSRM resistivity vs. depth profiling showed resistivity to be lower for SEI formed on native SiO_x, consistent with the greater relative composition of LiF. Resistivity measurements of the underlying Si showed that resistivity decreases after the first cycle, but increases after 10 cycles for native SiO_x, while resistivity of Si from the 5-nm SiO_2 sample showed little to no change through cycling. AFM morphology investigation showed an increase in surface roughness for SEI formed on native SiO_x after one cycle, with a restoration of a smooth surface after 10 cycles. Surface morphology of SEI formed on 5-nm SiO_2 showed little change through cycling, maintaining a smooth surface.

Reference

[1] M. N. Obrovac, L. Christensen, Electrochemical and Solid-State Letters 7 (2004) A93-A96.
[2] M. N. Obrovac, L. J. Krause, J. ELECTROCHEM. SOC. 154 (2007) A103-A108.
[3] C. Stetson, T. Yoon, J. Coyle, W. Nemeth, M. Young, A. Norman, S. Pylypenko, C. Ban, C.S. Jiang, M. Al-Jassim, A. Burrell, *Nano Energy* 55 (**2019**).
[4] E. Pollak, G. Salitra, V. Baranchugov, D. Aurbach, *J. Phys. Chem. C* 111 (**2007**) 11437–11444.

Understanding and Design of the Si SEI from Coupled Molecular Dynamics – First-principles Calculations (UC Berkeley)

Kristin Persson, Sang-Won Park, Tingzheng Hou (UC Berkeley)

Background

Our examination of the Si anode reactions includes modeling of the solvation structures within the bulk electrolyte and at the interfacial. Fluoroethylene carbonate (FEC) was recently proposed as an effective electrolyte additive that significantly enhances the stability and flexibility of the solid electrolyte interphase (SEI) layer for Si anodes. However, uncertainties still remain on the exact mechanism through which FEC alters the electrolyte decomposition and SEI formation mechanism. Dangling bonds of silica surface can be ionized, and the degree of ionization varies depending on the pH values in electrolyte and the size of silicon nano-particles, affecting SEI formation by changing the electric potential and Li^+ ions distribution at the surface. Herein, the influence of FEC on $LiPF_6$/EC electrolytes for Si anodes and the dependence of silica surface ionization on the electric potential is investigated through classical molecular dynamics (MD) simulations and quantum chemical calculations.

Results

The reduction potentials of free EC and FEC, their corresponding Li^+(solvent) complexes, and Li^+-PF6^- (solvent) complexes were investigated at the B3LYP/6-31+g(d) level of theory (Table 1). To effectively compare with experimental results, the calculated potential values were convoluted with an arbitrary 0.1 V width concave triangular wave, and plotted together with the experimental differential capacity (dQ/dV) versus potential (V) profile (Figure 1) [1]. The reduction products after geometry optimization were further scrutinized through spin density analysis to elucidate the reduction reaction process (Figure 2). The free EC molecule exhibits a calculated reduction potential of 0.21 V, with most of the extra electron residing on the O=CO(O) moiety which consequently deforms out of plane. According to Natural Bond Orbital (NBO) analysis, the C atom hybridization state changes from $sp^{2.0}$ to $sp^{2.6}$ to accommodate the extra e^-. The coordinated EC exhibits an increased reduction potential of 0.44 V–0.59 V (within 0.15 V), as compared with the uncoordinated molecule, which contributes to a broadening of the reduction peaks in the differential capacity plot. The obtained reduction potential is in good agreement with the previously obtained value of 0.53 V by G4MP2. Furthermore, the electron density of the reduced coordinated EC resides in the same region (e.g., on the O=CO(O)) as compared to the uncoordinated reduced EC. (Figure 2c, h, i, k, and l). We find weak to little dependence of the reduction potential on the number of explicitly coordinating solvents [2], e.g., the calculated corresponding reduction potentials are 0.50 V and 0.59 V for 5- and 6- fold structures (Figure 2k, and l), respectively.

When Li^+ is in direct coordination with FEC, the predicted FEC reduction potential is obtained as 0.81 V–0. 91 V, which is about 0.3 V higher than uncoordinated FEC. The calculated reduction potentials are in good agreement with the previous G4MP2 calculations (0.90 V) and measured values (1.0 V) [3]. If we compare the reduction behavior of EC-containing species and FEC-containing species, even the uncoordinated FEC exhibits a higher reduction potential than all investigated EC species, indicating a preferential reduction for FEC vs EC—for both minority as well as majority species. While the optimized FEC reduction products (Figure 2b, d, j, and m) exhibit the same electron distributions as its EC counterparts, the stronger exothermic nature of the FEC reduction indicates that these FEC-derivative species are sufficiently metastable to decay through reactions other than the C−O bond ring-opening of EC. This major mechanistic difference between the non-fluorinated and fluorinated carbonates allows for the recombination of fragments and intramolecular electron migration, facilitating the subsequent polymerization and LiF formation. We also note that, as Li^+-coordinated FEC minority species are decomposing at higher potentials, the bulk equilibrium will shift to maintain the population, hence supplying the reaction. Previous DFT calculations have shown that the additional F fragments from FEC decomposition exhibit a "glue effect" by strongly binding to Li atoms of multiple organic species and connecting them, leading to a more compact and stable SEI.
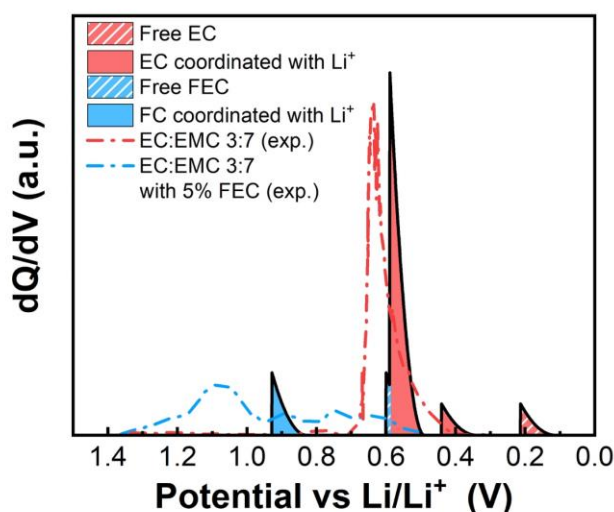
Figure 1. The calculated anticipated (solid line) and experimental (dash dotted line) differential capacity plots (dQ/dV vs. V) during the formation step of EC and FEC electrolyte. The computed profile is obtained by convoluting the calculated reduction potentials with a 0.1 V width concave triangular wave, the experimental one is reproduced from Xia, et al. [1] by removing the background.

Table-1: The reduction potential vs Li+/Li(s) (i.e. subtract 1.4 V) of individual solvent molecules and solvate complexes, in Volt.

Structures	Reduction potential
$EC + e^- \rightarrow EC^-$	0.21 V
$FEC + e^- \rightarrow FEC^-$	0.59 V
$Li^+-EC + e^- \rightarrow Li^+-(EC)^-$	0.54 V
$Li^+-FEC + e^- \rightarrow Li^+-(FEC)^-$	0.90 V
$Li^+-(EC)_4 + e^- \rightarrow Li^+-(EC)_3(EC)^-$	0.49 V
$Li^+-(EC)_3(FEC) + e^- \rightarrow Li^+-(EC)_2(FEC)(EC)^-$	0.55 V
$Li^+-(EC)_3(FEC) + e^- \rightarrow Li^+-(EC)_3(FEC)^-$	0.91 V
$Li^+-(EC)_5 + e^- \rightarrow Li^+-(EC)_3(EC)^- + EC$	0.50 V
$Li^+-(EC)_6 + e^- \rightarrow Li^+-(EC)_3(EC)^- + 2EC$	0.59 V
$Li^+-(EC)_5(FEC) + e^- \rightarrow Li^+-(EC)_3(FEC)^- + 2EC$	0.81 V
$Li^+-PF_6^- + e^- \rightarrow Li^+-F^- + PF_5^-$	spontaneous bond breaking
$Li^+-PF_6^-(EC) + e^- \rightarrow Li^+-PF_6^-(EC)^-$	0.59 V
$Li^+-PF_6^-(FEC) + e^- \rightarrow Li^+-PF_6^-(FEC)^-$	0.90 V
$Li^+-PF_6^-(EC)_5 + e^- \rightarrow Li^+-(EC)_3(EC)^- + PF_6^- + EC$	0.44 V

The reduction of the $Li^+-PF_6^-$ contact ion pair results in direct LiF formation. Upon geometry optimization, the PF_6^- structure is dynamically unstable, and the P−F bond spontaneously breaks to form PF_5^- and LiF (Figure 2e). However, the $Li^+-PF_6^-$ ion pair decomposition is expected to yield high reaction barrier at potential larger than 0.5 V [4]. When explicit solvent molecules are considered in the contact ion pair model, the reduction of the complex results in solvent reduction, elucidating that the decomposition of solvent molecules are preferred over that of the ion-paired PF_6^- (Figure 2f, g, and n), with similar reduction potential as SSIP structures. Thus, the reduction of PF_6^- is not expected to occur at a high potential, but may only occur during the initial stage of SEI formation if the anode is at sufficiently low potential [4].
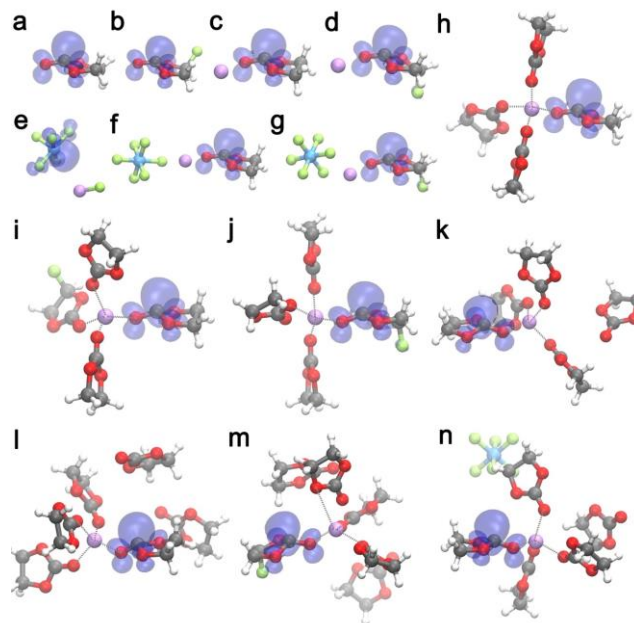
Figure 2. Geometries and spin density analysis of reduced solvent molecules (a) EC, (b) FEC, and solvate complexes (c) Li$^+$−EC, (d) Li$^+$−FEC, (e) Li$^+$−PF$_6^-$, (f) Li$^+$−PF$_6^-$(EC), (g) Li$^+$−PF$_6^-$(FEC), (h) Li$^+$−(EC)$_4$, (i) Li$^+$−(EC)$_3$(FEC) (EC reduction), (j) Li$^+$−(EC)$_3$(FEC) (FEC reduction), (k) Li$^+$−(EC)$_5$, (l) Li$^+$−(EC)$_6$, (m) Li$^+$−(EC)$_5$(FEC) (FEC reduction), and (n) Li$^+$−PF$_6^-$(EC)$_5$.

In order to study the liquid structure at amorphous silica surface, we initially used a simple model (CLAYYFF) for the amorphous silica layer consisting of only Lennard-Jones and Coulomb interactions, as previously used for bulk and surface crystalline silica.[5] To examine the effect of protonation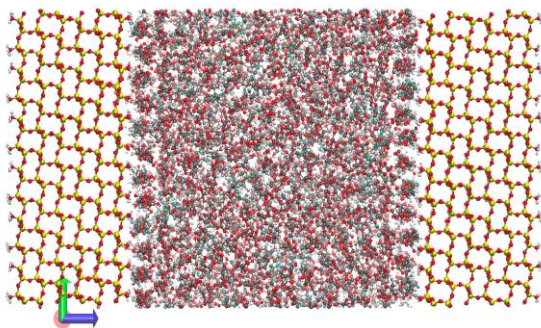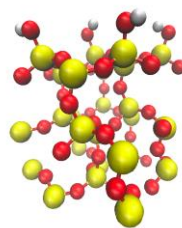 of the silica surface we employ a force field, INTERFACE FF.[6] This force field is optimized for a protonated silica surface, and we apply it to alpha-cristobalite ($10\bar{1}$), with all silanol groups protonated.

Figure 3. **(left)** Snapshot of simulation of silica interface with 1 M LiPF6/EC. Left/right electrodes are negatively/positively charged for ionized silica cases. **(right)** Dangling bonds at surface are substituted with silanol groups. Area density of silanol groups is set to 4.5 nm^{-2}, and degree of ionization is varied from 0 to ~ 0.9 nm^{-2}, which is equivalent to 20% of surface silanol groups.

Silica surfaces are known to exhibit various values of "point of zero charge" (PZC), or isoelectric point (IEP) under different conditions, ranging from 1.6 to 6.3.[7] While PZC values for silica surfaces have been measured mostly in aqueous solution, to our knowledge, silica surfaces in aprotic solvents, such as ethylene carbonate, have not

been rigorously studied. Here we study general trends of the electrical properties of a silica surface in 1 M LiPF$_6$/EC, by changing surface condition of the silica, crystalline to amorphous, and increasing the degree of ionization of the surface silanol groups (Figure 3). MD simulations for this study are performed with Gromacs code and the trajectories are obtained at 350 K.

The number of Li ions at the surface, N_{Li}, is shown in Figure 4**a**. We note that the behavior of N_{Li} as a function of ionization mimics that of the electric double layer potential since the electrolyte counter ion population screen the electrode charges. The electric potential, $\Phi(z)$, is obtained by integrating the Poisson equation

$$\Phi(z) = -4\pi \sum_\alpha \int_{-z_0}^{z} dz'(z-z')\bar{\rho}_\alpha(z'); \quad \bar{\rho}_\alpha(z) = A_0^{-1} \int_{-x_0}^{x_0} \int_{-y_0}^{y_0} dx'dy'\rho\_\alpha(x',y',z),$$

where $\bar{\rho}_\alpha(z)$ is the charge density profile in 1D, i.e., along the z axis. Figure 4**b** shows the electric potential profile, $\Phi(z)$, at 0, 0.8, 3.3, 10, and 20% ionized silica surfaces, where the ionization is enabled simply by adding a (somewhat artificial) homogeneous negative charge. The 0% ionized silica surface exhibits a net zero charge in the bulk silica, and the electric potential difference between the bulk and the surface is defined as the "potential of zero charge", which is equal to the electric potential of the surface with net zero charge. The resulting potential of zero charge is < 1 V (see the red curve in Figure 4**b**). However, we note that the electric potentials at the silica surfaces are unphysically high. The higher ionization degrees show linearly increasing potential in the bulk region, which is rationalized by a saturation of Li$^+$ at the surface, which incompletely screen the negative charges. We will improve the model by explicitly deprotonating the silanol groups and anticipate that the model study will elucidate the dependence of electrolyte speciation at the interface, and hence favorable electrolyte decomposition, on the degree of surface ionization and resulting electric double layer at the silica surface.
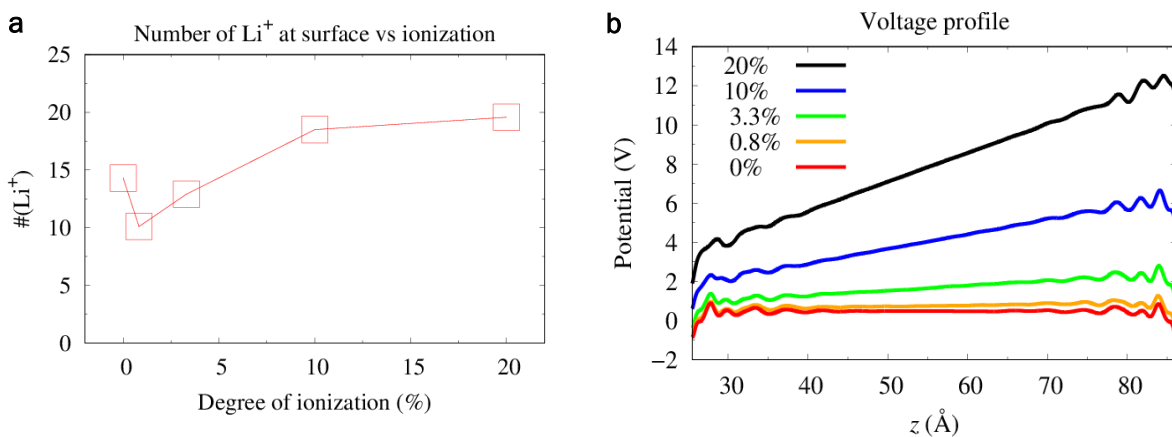

Figure 4. (**a**) Number of Li+ ions, N_{Li}, at the ionized silica surface vs. degree of ionization. N_{Li} seems to be saturated at 10% ionization. (**b**) The electric potential profile, $\Phi(z)$, with 0, 0.8, 3.3, 10, and 20% ionized, or neutral, 1, 4, 12, and 24 e charged. The neutral case indicates the "potential of zero charge" is in mV scale, which is within comparable to typical values. Electrode/electrolyte interfaces are formed at z = 25 Å (ionized electrodes, negatively charged) and 86 Å (positive counter electrode).

Conclusions

1. Li$^+$-coordinated FEC exhibit higher reduction potential than corresponding EC species, and contributes to an early onset of anode SEI formation and passivation. Preferred reduction of FEC introduces a higher ratio of LiF to the SEI.
2. The exothermic nature of the FEC reduction also supports the reported reaction pathway of defluorination and subsequent polymerization.
3. Simulation of the electric double layer potential and total number of Li+ ions at the silica surface with different degrees of ionization is obtained. Improved models with deprotonated surface silanol groups are forthcoming.

References

[1] J. Xia, R. Petibon, A. Xiao, W.M. Lamanna, J.R. Dahn, Some Fluorinated Carbonates as Electrolyte Additives for Li(Ni0.4Mn0.4Co0.2)O2/Graphite Pouch Cells, *J. Electrochem. Soc.*, 163 (2016) A1637-A1645.

[2] A. von Wald Cresce, O. Borodin, K. Xu, Correlating Li+ Solvation Sheath Structure with Interphasial Chemistry on Graphite, *J. Phys. Chem. C*, 116 (2012) 26111-26117.

[3] J. Xia, R. Petibon, D. Xiong, L. Ma, J.R. Dahn, Enabling linear alkyl carbonate electrolytes for high voltage Li-ion cells, *J. Power Sources*, 328 (2016) 124-135.

[4] K. Leung, Predicting the voltage dependence of interfacial electrochemical processes at lithium-intercalated graphite edge planes, *Phys Chem Chem Phys*, 17 (2015) 1637-1643.

[5] R. T. Cygan, J.-J. Liang, A. G. Kalinichev, Molecular Models of Hydroxide, Oxyhydroxide, and Clay Phases and the Development of a General Force Field, *J. Phys. Chem. B* 108 (2004) 1255–66.

[6] F. S. Emami, P. Valeria, R. J. Berry, V. Varshney, S. V. Patwardhan, C. C. Perry, H. Heinz, Force Field and a Surface Model Database for Silica to Simulate Interfacial Properties in Atomic Resolution, *Chem. of Mater.* 26, (2014) 2647-2658.

[7] M. Kosmulski, pH-Dependent Surface Charging and Points of Zero Charge. IV. Update and New Approach, *J. Colloid Interface Sci.* 337 (2009): 439–48.

SEISta – Fluorescent probes (NREL)   (FY19 Q1)

Contributors (NREL – Wade Braunecker)

Background

During FY18, new Li ion fluorescent probes were developed from literature analogues that could be covalently tethered into polymeric systems commonly employed as binder materials or in polymer electrolytes. Some initial characterization was performed to demonstrate the sensitivity of this probe's absorbance spectra to Li ion concentration in solution, and several different sensors were developed with a wide range of absorbance onsets and tunable emission spectra. At the end of FY18, we had just begun studying the potential to use these materials to "stain" conductive surfaces in an attempt to measure/image Li ion flow across the SEI in order to assess how heterogeneities in Li ion concentration developed during cycling. Here we report on our progress towards that goal in Q1 of FY19, including our study of the fluorescent properties of the compounds under different relevant conditions (under basic vs. pH neutral vs. acidic conditions; fluorophores with electron donating vs. withdrawing groups; solution vs. solid state fluorescence). These results will help us design an appropriate "stain" to apply to the SEI.

Results

1) Fluorescence response at varying pH. This was important to investigate as literature reports generally employed these fluorescent sensors under pH basic conditions, where the hydroxyl group is deprotonated to bind Li, and their sensitivity under neutral or acidic conditions (*i.e.,* in the presence of polyacrylic acid) was unclear. The fluorescence response of the vinyl (hydroxyphenyl)napthoxazole (HPNO) monomer (see top of Figure 1) was first investigated in neutral propylene carbonate (PC). As can be seen in Figure 1C, there is a very weak fluorescence response under pH neutral conditions (1 eq. of LiTFSI increases fluorescence by only ~30%, and 100 eq. are required to double fluorescence). Under basic conditions (0.25 M triethylamine), the fluorescent sensor is significantly more sensitive (by nearly two orders of magnitude), with fluorescence doubling in the presence of just ½ eq. of Li, and increasing 4-fold in the presence of just 10 eq. of Li. "Slightly" basic conditions were also tested using 25 eq. of pyridine (as might be introduced in a poly(vinyl pyridine) binder). Fluorescent sensitivity was intermediate to the aforementioned two systems. In the presence of 0.025 M acrylic acid, there is no fluorescence response until very high Li concentrations. The results indicate more sensitive fluorescent "stains" will require the presence of some added base.

a) Absorbance w/ & w/o Li⁺

b) Fluorescence w/ increasing Li⁺

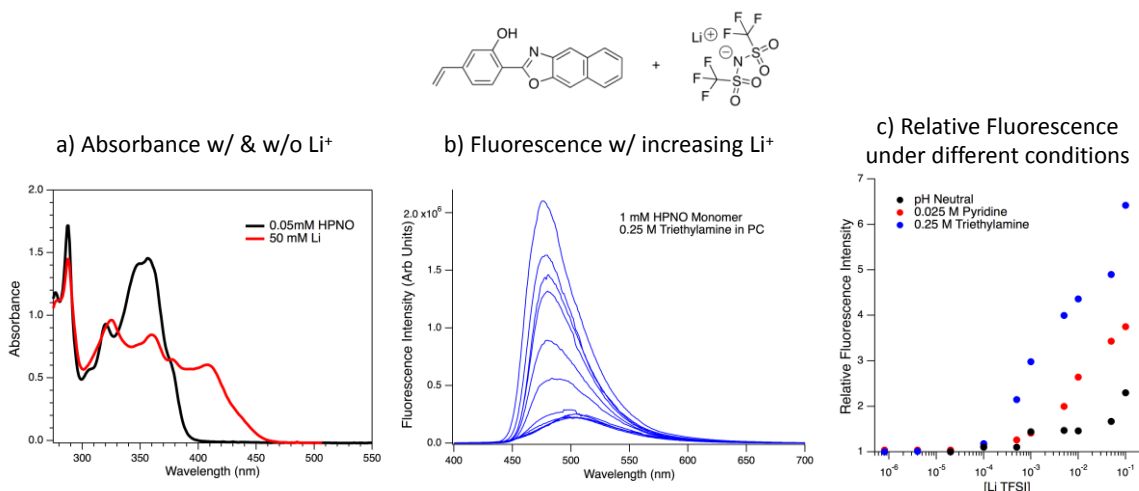c) Relative Fluorescence under different conditions

Figure 1. A) Absorbance spectrum of 0.05 mM HPNO in propylene carbonate (black trace) and large excess of LiTFSI (red trace). B) Fluorescence intensity of 1 mM HPNO in PC and 0.25M triethylamine recorded as a function of increasing LiTFSI concentration (0.01mM Li to 100 mM Li). Excitation at 330 nm. C) Relative fluorescence (integrated signal) of HPNO under neutral conditions, 0.025 M pyridine, and 0.25 M triethylamine.

2) Fluorescence response in presence of electron withdrawing groups (EWG). We previously developed (see FY18 annual report) an analogue of the HPNO monomer with strong EWGs that dramatically red-shifted absorption and reportedly had a fluorescence response out to ~ 750 nm. This was originally pursued to give us the ability to tune emission should it overlap with other fluorescent materials in a battery (e.g., graphene).

Although the binding of Li to this sensor does dramatically change its absorbance spectrum relative to that of the unbound sensor, unfortunately, fluorescence does not "turn on" in the same way it does for the HPNO monomer depicted above in Figure 1, and in fact is even slightly quenched. Thus, we will abandon this class of materials with EWGs and focus only on more promising fluorophores with electron donating groups in future studies.

3) Design of fluorescent "stain". We made some initial crude attempts to deposit the HPNO monomer as a stain, as well as a polymethylacrylate polymer with 2 mol% HPNO covalently bound, onto a conductive FTO substrate for some
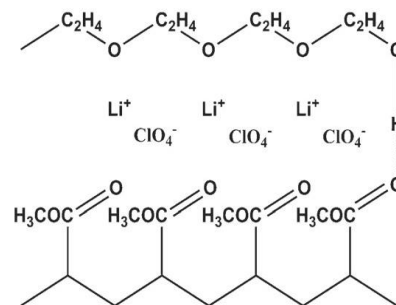
Figure 2. PMA/PEG-based gel electrolyte

initial spectroelectrochemical measurements with and without Li. There were numerous problems encountered, most notably that the stain would simply dissolve into most electrolyte systems, or the polymeric film would not be sufficiently conductive.

We are currently synthesizing an analogue of a literature polymer gel electrolyte. The literature system is composed of PEO, PMA, $LiClO_4$, and ~50 volume % DMSO. At 80 C, this electrolyte flows like a liquid, but becomes a solid gel at room temperature. Our electrolyte gel will contain Na ions and PMA with 2 mol% HPNO. HPNO has no fluorescence response to Na ions. Our system will also ideally incorporate some base (in the form of vinyl pyridine?). This system will allow us in principle to flow/deposit a homogeneous layer of conductive gel electrolyte onto the SEI layer at high temperatures; afterwards, we will cool the electrolyte to "fix" it in place and attempt to cycle the system one time and drive Li from the anode through the SEI and into our electrolyte gel, with the goal of ultimately imaging the flow of Li through our fluorophore containing electrolyte as it displaces Na. We will be coordinating with other SEISta researchers to efficiently develop a preparatory procedure that does not damage the fragile SEI layer during this procedure.

Conclusions

Significant progress was made toward developing Li ion sensors for application as a fluorescent "stain" on an SEI layer. We have a better understanding of conditions required to sense/image Li, and we have begun developing a gel electrolyte for this purpose.